BUTTERWORTH HEINEMANN

Polymer Vol. 36 No. 1, pp. 109–127, 1995

0032-3861/95/$10.00 + 0.00

Structure and mass transport in constrained polymer crystals via molecular dynamics simulations

G. L. Liang, D. W. Noid, B. G. Sumpter and B. Wunderlich*
Chemical and Analytical Sciences Division, Oak Ridge National Laboratory, Oak Ridge, TN 37831-6197, USA, and Department of Chemistry, The University of Tennessee, Knoxville, TN 37996-1600, USA
(Received 3 February 1994; revised 18 April 1994)

To study the plastic deformation of polymer crystals, the structure and molecular motion in surface-constrained polymethylene crystals containing 192 $C_{50}H_{100}$ chains were followed using molecular dynamics simulations. Total energy, temperature and density were evaluated as a function of time up to 100 ps. Structure changes, longitudinal and transverse mass transport, changes in setting angle of the zigzag chains and the concentration and distribution of *gauche* conformations were noted. Selected chains were followed during the plastic deformation by tracing their centre-of-mass coordinates and end-to-end distances. The plastic deformation involves affine expansion and contraction, development of crystallographic fault lines (slip planes), edge dislocations, curved lattice planes and longitudinal diffusion of chains out of the crystal. The time-scale for all these motions is in the picosecond range. The actual chain motion reaches about 10% of the speed of sound.

(Keywords: conformational defect; molecular dynamics; molecular motion)

INTRODUCTION

In polymeric materials, details of molecular mobility are essential to elucidate mechanisms of crystallization, annealing, deformation and melting[1]. Only recently has it become possible to model whole crystals realistically using supercomputers. In this paper we describe for the first time the molecular dynamics simulation of the large-amplitude motion necessary for plastic deformation. For this purpose the simulated crystal is partially constrained and its flow out of or into the enclosure by imposing large temperature changes is followed.

A brief review of the growth of our knowledge about defects in polyethylene and paraffins is given next to enable an appreciation of the progress made possible by large-volume molecular dynamics simulations. Only the extreme slowing of motion that can be achieved by use of a supercomputer allows us to follow the picosecond (10^{-12} s) processes basic to the large-amplitude motion of molecules.

Rotation of the whole chain was the earliest model for large-amplitude motion in paraffin crystals. It was proposed by Müller in 1932 to explain the hexagonal crystal phase ('rotator phase')[2,3]. Most later suggestions of large-amplitude motion were also based on experimental observations, such as i.r., Raman and n.m.r. spectroscopy and X-ray diffraction, neutron-scattering and dielectric measurements[4–13]. Early n.m.r. data on the 'rotator phase' of $C_{32}H_{66}$ were interpreted by Olf and Peterlin[5] to result from molecular motion based on rotation coupled with longitudinal translation. All molecules in the crystal were found to participate in the motion. Later, X-ray diffraction, neutron-scattering and dielectric measurements, as well as i.r., Raman and n.m.r. spectroscopy, of $C_{33}H_{68}$ by Strobl and coworkers[6–8] showed that the rotational disorder destroys the sublattice structure. The rotational 180° jumps interrupt the long-range order of the zigzag skeletal plane, but a short-range order was proven to be preserved. Screw jumps were suggested to be superimposed on the chain rotation and the cause of longitudinal shifts. In addition, the introduction of intrachain defects with diffusion along the chains was suggested to enhance the mobility. Specific temperature ranges were given for each of the motions. Neutron-scattering studies of paraffins also pointed to substantial translational and rotational diffusion[9–11]. New results of X-ray diffraction and differential scanning calorimetry (d.s.c.) by Ungar[12] also support the view that all molecules are equivalent in the 'rotator phase'. It must be noted, however, that the diffraction experiments give information on long-time/wide-range averages of molecular orientations, whereas i.r., Raman and n.m.r. spectroscopy may be fast enough to resolve instantaneous differences. The spectroscopic methods thus reveal that the 'rotator phase' does not have equivalent local arrangements[12]. The non-equivalence supports crystals with different domains, as has been suggested by X-ray

* To whom correspondence should be addressed at the Department of Chemistry, The University of Tennessee, Knoxville, TN 37996-1600, USA

diffraction, i.r. and Raman spectroscopy, and also differential scanning calorimetry on solid solutions of heneicosane ($C_{21}H_{44}$) and tricosane ($C_{23}H_{48}$)[13]. Each domain is ordered, encompassing tens of molecules in which each chain has only four equivalent orientations around its chain axis with negligible conformational disorder[14].

Initial computational research on large-amplitude motion in polymers and paraffins made use of Monte Carlo (MC), limited molecular dynamics (MD) and molecular mechanics (MM) methods. The MC simulations of paraffins by Yamamoto[15,16] used chains that were assumed to be rigid and all-*trans*. These simulations suggested that the 'rotator phase' has a domain structure within which the chains tend to align parallel with their zigzag planes[15]. The overall molecular motion in the 'rotator phase' has been described in terms of the movement of the boundaries of the ordered domains[16]. Ryckaert *et al.*[17] carried out MD simulations simplified by either periodic boundary conditions in the chain direction or small bilayer crystals of tricosane (30 chains in each crystal layer). Furthermore, the molecular chains in the 'rotator phase' were permitted only four well-defined orientations (setting angles). The longitudinal-translational and rotational diffusions were indeed found to be of the jump type and translation was found to occur at a lower temperature than rotation without coupling between the two[17,18]. Molecular mechanics calculations of the isolated chain and within the crystal led to the description of point defects and suggestions of their contribution to large deformations were made. Kink[19] motion and soft twists[20,21] have been proposed for longitudional-translational motion in polymer crystals.

To assess the influence of all modes of motion within a chain and with its neighbours, detailed MD studies of crystals with sizes approaching experimental crystals are necessary. Such studies were only recently possible using large-scale MD simulations on unconstrained crystals of long methylene sequences[22–27]. These simulations revealed that the dominant motion in the hexagonal 'rotator phase' is a picosecond time-scale segmental twist that is coupled with intramolecular transverse, longitudinal and torsional as well as long-wavelength intermolecular transverse vibrations. The crystal structure consists of dynamic, nanometre-scale domains with a lower-symmetry packing. Changes in the domain structure can be linked to the crystal volume vibration modes[24]. This description is in good agreement with the experiments and removes many of the contradictions present in earlier models.

In addition to resolving the crystal structure it is possible to use MD simulations to study superheating above the melting temperature. This results in surface melting of the crystal, initiated also on a picosecond time-scale[25]. This rapid molecular motion, when unconstrained by surrounding crystals, is slowed by the cooperative motion necessary for a melt surface to penetrate into the crystal. Linear melting rates of polyethylene crystals are enormously slower. Experiments result typically in linear melting rates of $5\Delta T\mu m\,K^{-1}\,s^{-1}$, where ΔT is the superheating[28].

The details of kink and twist motion and their influence on single-chain diffusion can also be clarified by MD simulations[29]. The mechanism of defect formation needs a cooperative action of all skeletal vibrations. Chain diffusion may be enhanced by the presence of kinks, but the kinks themselves are not mobile. A detailed review of these results is given elsewhere[22].

The MD simulations have thus been able to give information on some of the most difficult problems of the solid state of polymers. The present simulations were designed to explore larger-scale deformations of crystals by placing them in surface constraints of too small or too large a volume and following the plastic deformation. Three types of constraints were chosen: (1) four-sided, full lateral surface constraints (4-SC); (2) three-sided, partial lateral surface constraints (3-SC); and (3) two-sided corner constraints (2-SC). The 4-SC permit the study of longitudinal diffusion of the chains out of the region of high pressure caused by the constraint. The 2-SC permit the study of lateral motion during attainment of the steady state. The MD simulations of our laboratory are distinguished from prior work of other authors by the absence of periodic boundary conditions. The united atom (UA) model was used for the simulation. A limited number of simulations that include the hydrogen atoms have also been carried out. Their results and limitations are described and discussed elsewhere[27]. The UA model uses considerably less computer time and yields many results that are in accord with experimental data, and furthermore permits comparison with our extensive earlier UA simulations[23–27].

COMPUTATIONAL METHODS

The simulations were carried out starting with CH_2 chains in perfect orthorhombic (ORTH) or monoclinic (MONO) structures, illustrated in the x–y projections of *Figure 1*. The double crosses mark the zigzag positions of the carbon atoms in the all-*trans* chains. The experimental room-temperature lattice parameters of polyethylene were used as initial crystal structures: for ORTH, $a=0.74$, $b=0.49$ and $c=0.25$ nm with c being the chain axis[30]; and for MONO, $a=0.81$, $b=0.25$ and $c=0.48$ nm and $\beta=108°$ with b being the chain axis[31]. Note that for the ORTH crystal in *Figure 1*, a, b and c are parallel to x, y and z, while the MONO crystal has a and b parallel to x and z and c is 18° off the y direction. In *Figure 1* each crystal contains 192 chains each consisting of 50 CH_2 groups, i.e. there are 9600 CH_2 groups with an initial dimension of about $6.0\times6.0\times6.3\approx227$ nm^3. Stretching, bending and torsional motion are allowed for all dynamic chains. The indices (i and j) in *Figure 1* indicate the position for each chain. The chains in the area between two rectangles are considered to be surface chains and could be frozen in the simulation, depending on the type of constraint. The frozen chains are not permitted to participate in any motion, but contribute to the van der Waals interactions with the dynamic chains.

The Lagrangian operator $\mathscr{L}$ for the system is described as

$$\begin{aligned}\mathscr{L}=&\sum_{i=1}^{N}\frac{1}{2}(m\dot{x}_i^2+m\dot{y}_i^2+m\dot{z}_i^2)\\&-\sum_{l=1}^{M}\sum_{i=1}^{49}V_{2b}(r_{i,i+1})-\sum_{l=1}^{M}\sum_{i=1}^{48}V_{3b}(\theta_{i,i+1,i+2})\\&-\sum_{l=1}^{M}\sum_{i=1}^{47}V_{4b}(\cos\tau_{i,i+1,i+2,i+3})-\sum_{i+j\geq4}^{N}V_{NB}(r_{ij})\end{aligned}\qquad(1)$$

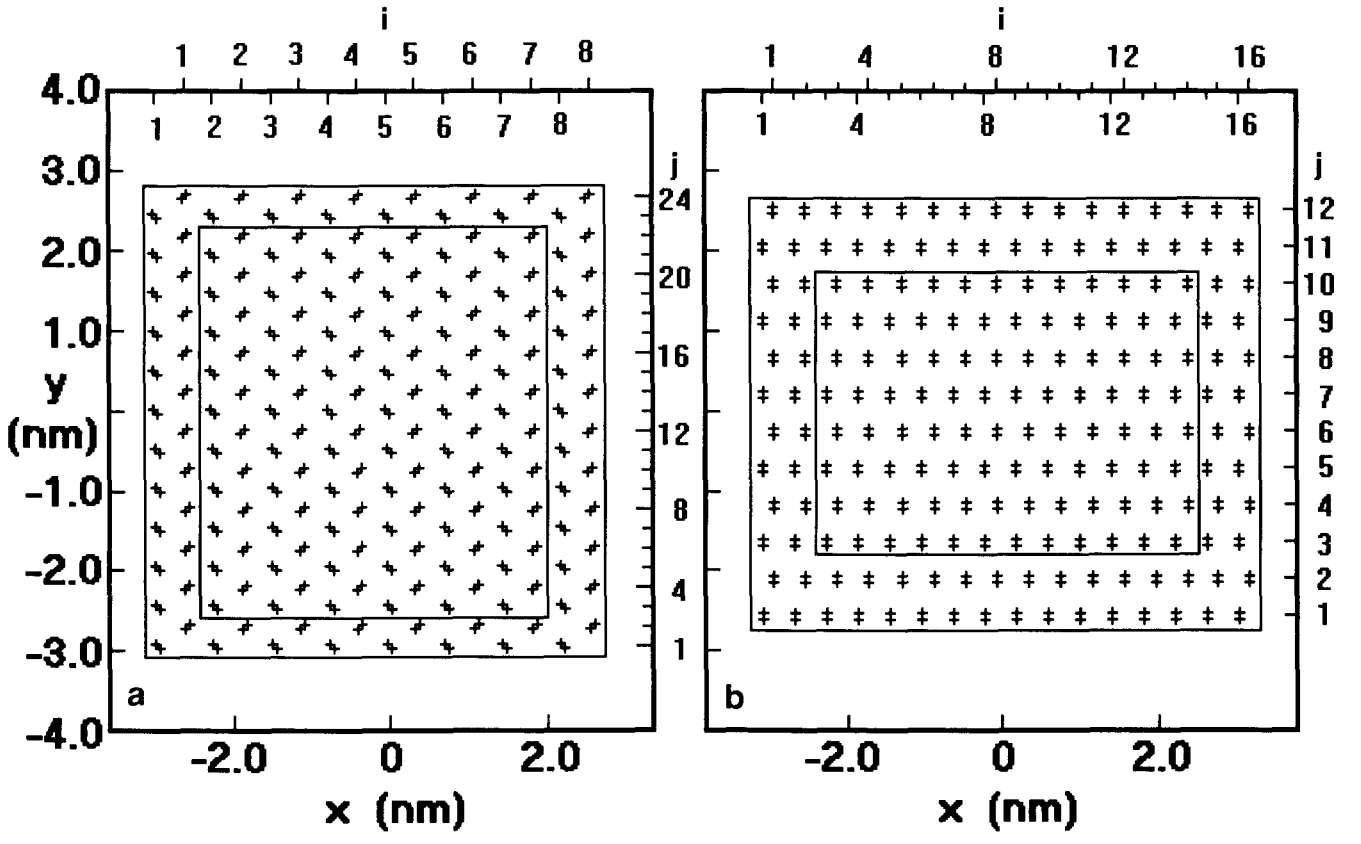

Figure 1 Two-dimensional representations of the initial crystal structures (the indices i and j label each chain): (a) orthorhombic (ORTH); (b) monoclinic (MONO)

Table 1 Force field parameters

Two-body interactions	Four-body interactions
$D = 334.72$ kJ mol^{-1}	$a = 18.41$ kJ mol^{-1}
$r_e = 0.153$ nm	$b = 26.78$ kJ mol^{-1}
$\alpha = 19.9$ nm^{-1}	
Three-body interactions	Non-bonding interactions
$K_\theta = 130.22$ kJ mol^{-1}	$\varepsilon = 0.477$ kJ mol^{-1}
$\theta_0 = 113°$	$\sigma = 0.398$ nm

in which N is the total number of dynamic CH_2 groups and M is the number of dynamic chains in the crystal depending on the type of constraint, 2b, 3b and 4b represent the two-body (stretching)[32], three-body (bending)[33] and four-body (torsional)[34,35] interactions, respectively, and NB represents the non-bonding interactions[36]:

$$V_{2b}(r_{i,i+1}) = D\{1 - \exp[-\alpha(r_{i,i+1} - r_e)]\}^2 \quad (2)$$

$$V_{3b}(\theta_{i,i+1,i+2}) = \tfrac{1}{2}K_\theta(\cos\theta_{i,i+1,i+2} - \cos\theta_0)^2 \quad (3)$$

$$V_{4b}(\cos\tau_{i,i+1,i+2,i+3}) = 8.37 - a\cos\tau_{i,i+1,i+2,i+3} + b\cos^3\tau_{i,i+1,i+2,i+3} \quad (4)$$

$$V_{NB}(r_{ij}) = 4\varepsilon[(\sigma/r_{ij})^{12} - (\sigma/r_{ij})^6] \quad (5)$$

The parameters for equations (2)–(5) are listed in *Table 1*. These force field parameters have been well justified and commonly used for UA modelling of polyethylene[29,32–39].

To start the simulation, the crystals were heated by randomly adding kinetic energy to each CH_2 group in the dynamic chains arranged as in *Figure 1*. The simulations represent a microcanonical ensemble. The non-bonding interaction cut-off was set at 1.0 nm and the integration error was controlled to be less than 10^{-4}. The computational step size was adjusted automatically between 0 and 0.005 ps to reach the required precision. The neighbour list used for the calculation of the van der Waals interactions was updated every 0.05 ps during the simulations. Owing to the loss and gain of atoms in the neighbour list, the total energy decreased continuously and the temperature dropped during the simulation. This change in temperature was slow enough to occur without loss of steady state, as is shown below. The calculations took approximately 15 h of processor time per picosecond of simulation on a Cray X-MP computer. Further details on the programming strategy can be found elsewhere[40,41].

RESULTS

Energy, temperature and density

Six simulations were carried out with different types of initial structure, constraint and temperature. The characteristics of these runs are listed in *Table 2*. The total energy of the system was evaluated every 0.1 ps. *Figure 2* shows typical changes in total energy for runs S11, S13, S14 and S15.

The effective temperature of the simulation was calculated from the average kinetic energy in 0.1 ps

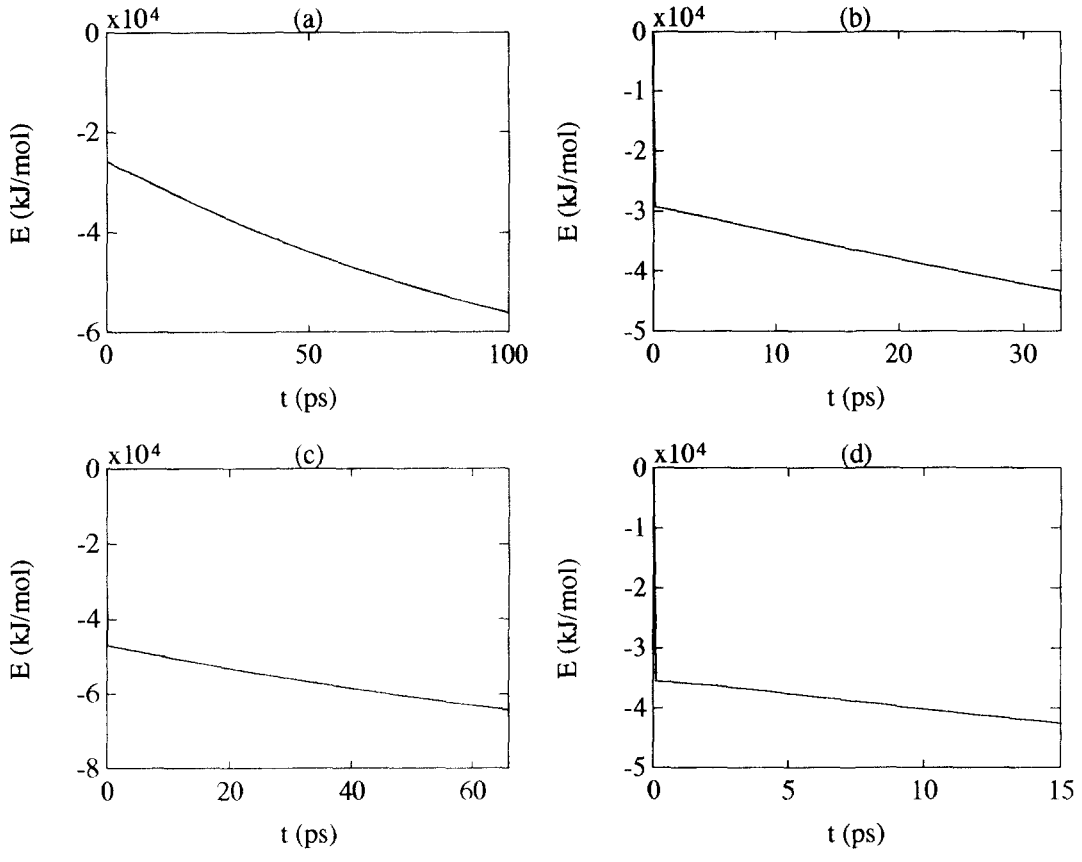

Figure 2 Total energy as a function of simulation time: (a) run S11; (b) run S13; (c) run S14; (d) run S15

Table 2 Times and temperature ranges in the simulations of superheated and constrained crystals

Run code	Crystal type	Constraint type	Time (ps)	Initial temperature[a] (K)	Final temperature[a] (K)
S10	MONO	4-SC	20	480	446
S11	MONO	3-SC	100	442	255
S12	MONO	3-SC	100	222	144
S13	ORTH	3-SC	33	457	359
S14	ORTH	4-SC	66	340	227
S15	ORTH	2-SC	15	435	379

[a] After 0.1 ps (at which the initial temperature is listed), the temperature decreases gradually. The final temperature is the temperature at which the simulation was stopped (corresponding to the given simulation time)

intervals using the relationship

$$\tfrac{3}{2}NkT=\tfrac{1}{2}m\sum_{i=1}^{N}(\dot{x}_i^2+\dot{y}_i^2+\dot{z}_i^2) \qquad (6)$$

where k is Boltzmann's constant, $\dot{x}_i$, $\dot{y}_i$ and $\dot{z}_i$ are the Cartesian velocities of the atoms i and N is the total number of dynamic CH_2 groups in the crystal. Parallel to the decrease in energy, a temperature decrease was observed in all simulations. *Figure 3* shows examples of temperature plots to be compared with the total energy changes in *Figure 2*.

The density of the interior of each crystal was averaged every 0.1 ps using a box-sampling method[24]. The dynamic atoms within a cubic box about the centre of the crystal with side dimensions increasing from 3 to 5 nm were counted. The results were plotted as a function of time, as shown in *Figure 4*. Depending on the type of constraint, different types of density fluctuation were observed. The densities of the initial ORTH and MONO crystals as illustrated in *Figure 1* were calculated with this method to be 1.02 g cm^{-3} and 0.98 g cm^{-3}, respectively.

Structure changes

The crystals with partial lateral surface constraint show changes in their structure and considerable mass transport. *Figures 5* and *6* are projections along the chain axes and reveal the disorder and lateral motion. *Figure 7* shows longitudinal mass transport for separate crystal layers for the case of full lateral surface constraint (4-SC). For a better understanding of the average crystal structures and to observe changes in setting angle, i.e. the angle between the zigzag plane and the crystal x–z plane, each chain was averaged and then plotted in an x–y projection. *Figures 8–12* show these plots at selected times for the simulations S11–S15.

The three-dimensional lattice parameters for the 4-SC crystal of simulation S14 are shown in *Table 3* using average single-atom lattice parameters and disregarding the setting angle of the chains. The lattice points were chosen at the centre between two adjacent CH_2 groups along the backbone chain. Their parameters are basically the same as in the initial ORTH structure of *Figure 1a* (0.49, 0.44 and 0.25 nm; 90°, 90° and 124°, respectively).

Conformational analysis

The main conformational defect is a *gauche* bond interrupting the all-*trans* sequence of the crystal. A *gauche* bond was counted as soon as a given bond deviated by

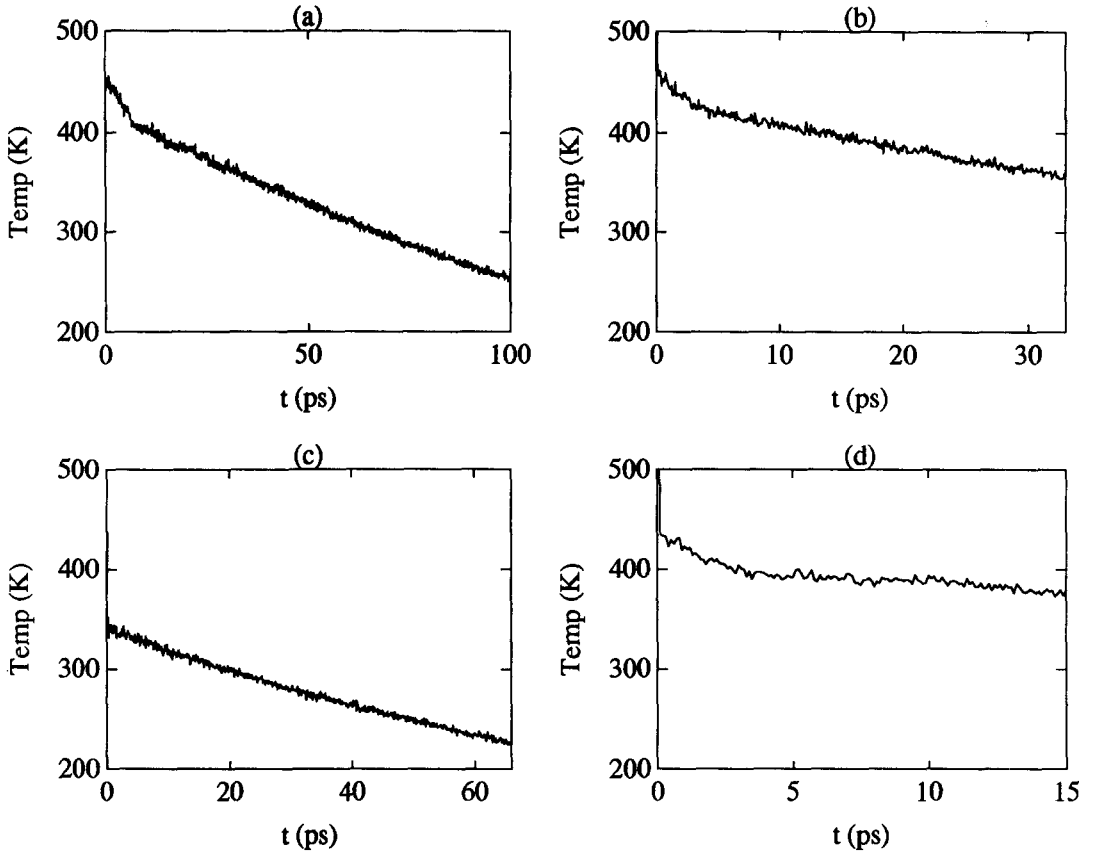

Figure 3 Temperature as a function of simulation time: (a) run S11; (b) run S13; (c) run S14; (d) run S15

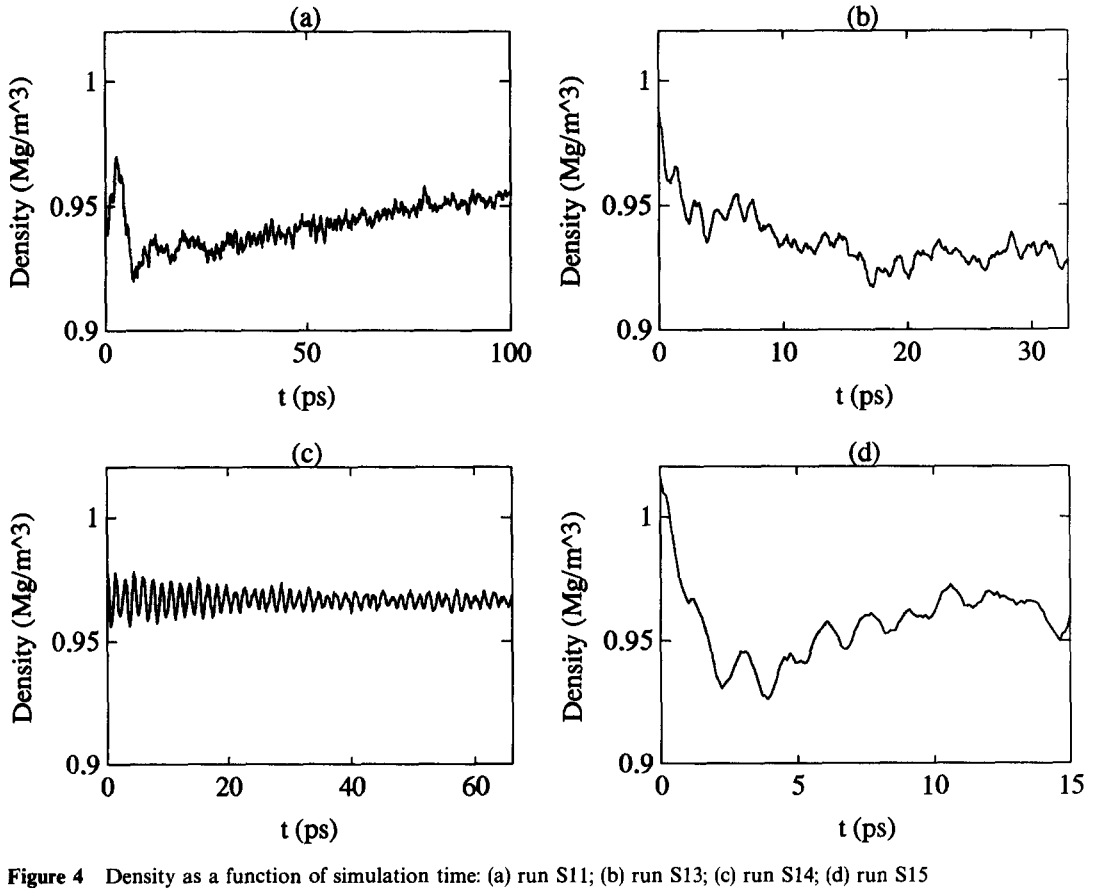

Figure 4 Density as a function of simulation time: (a) run S11; (b) run S13; (c) run S14; (d) run S15

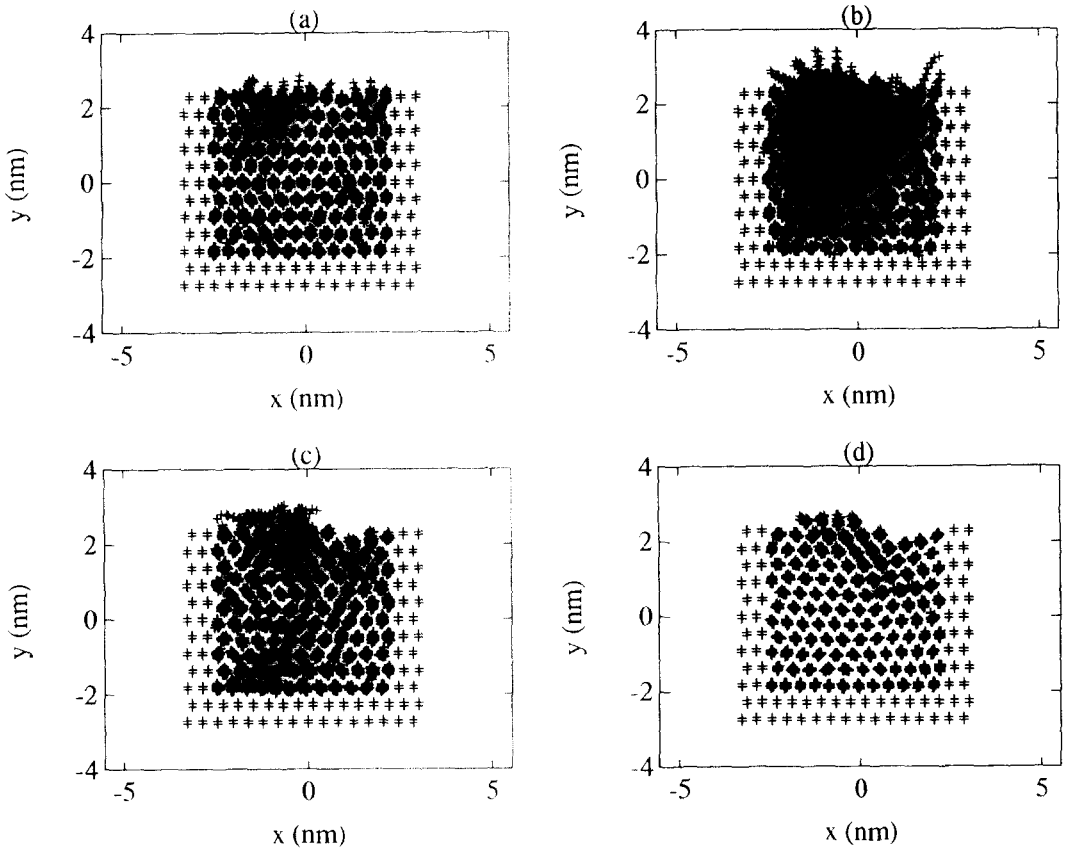

Figure 5 The x–y projections of the crystal in the simulation S11: (a) 1 ps, 450 K; (b) 5 ps, 421 K; (c) 30 ps, 363 K; (d) 100 ps, 255 K

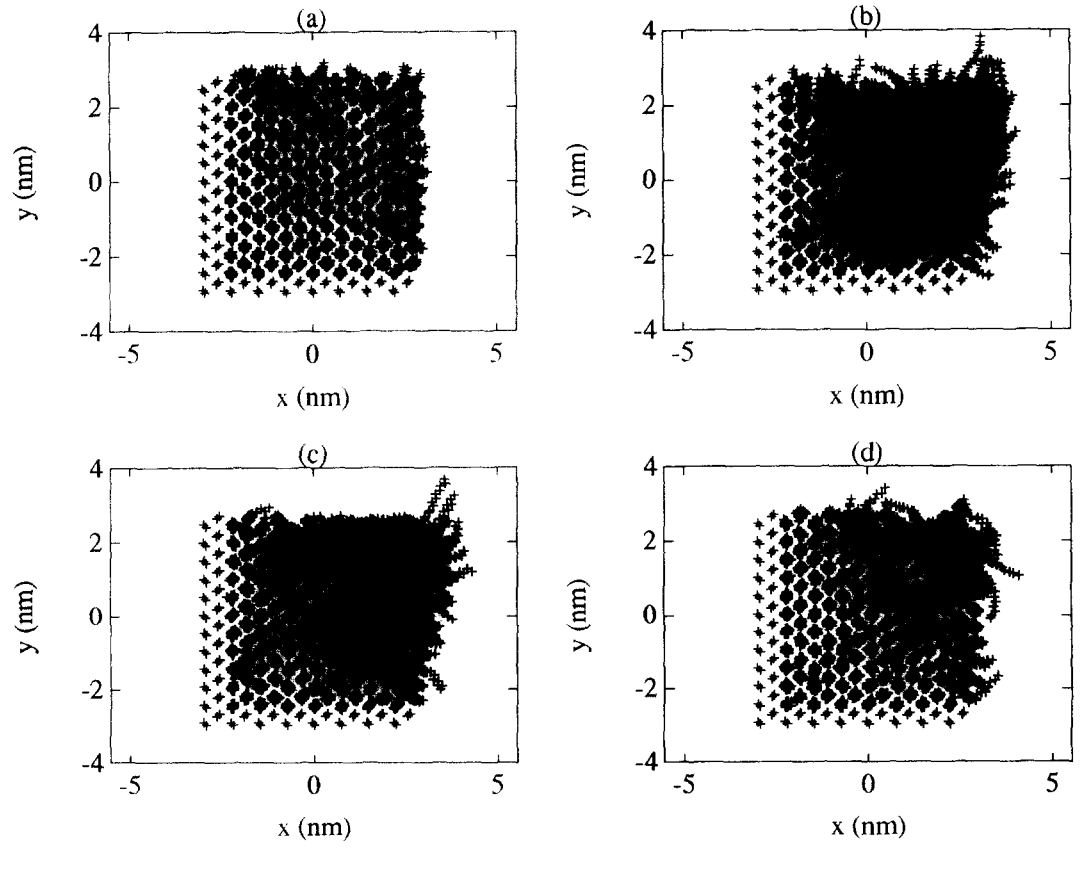

Figure 6 The x–y projections of the crystal in the simulation S15: (a) 1 ps, 423 K; (b) 6 ps, 394 K; (c) 10 ps, 393 K; (d) 15 ps, 379 K

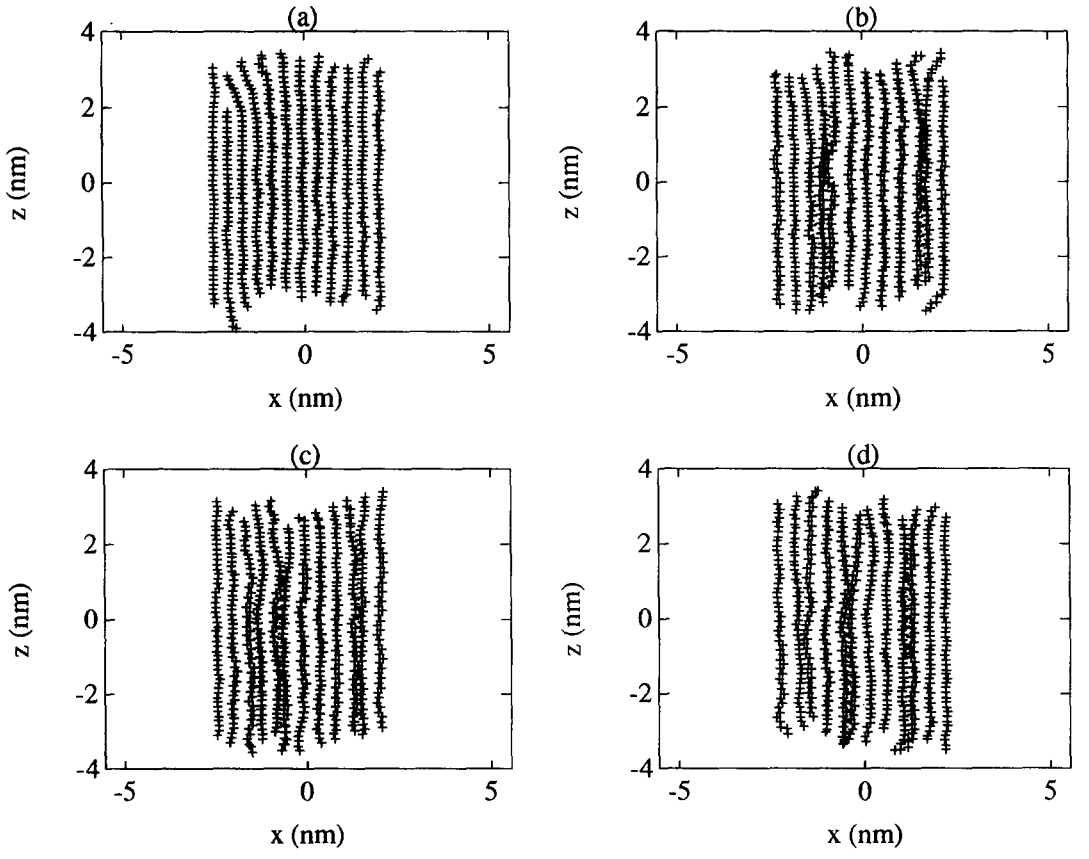

Figure 7 The x–z projections of the crystal in the simulation S10 at 10 ps: (a) layer $j=3$; (b) layer $j=6$; (c) layer $j=7$; (d) layer $j=8$ (see *Figure 1a*)

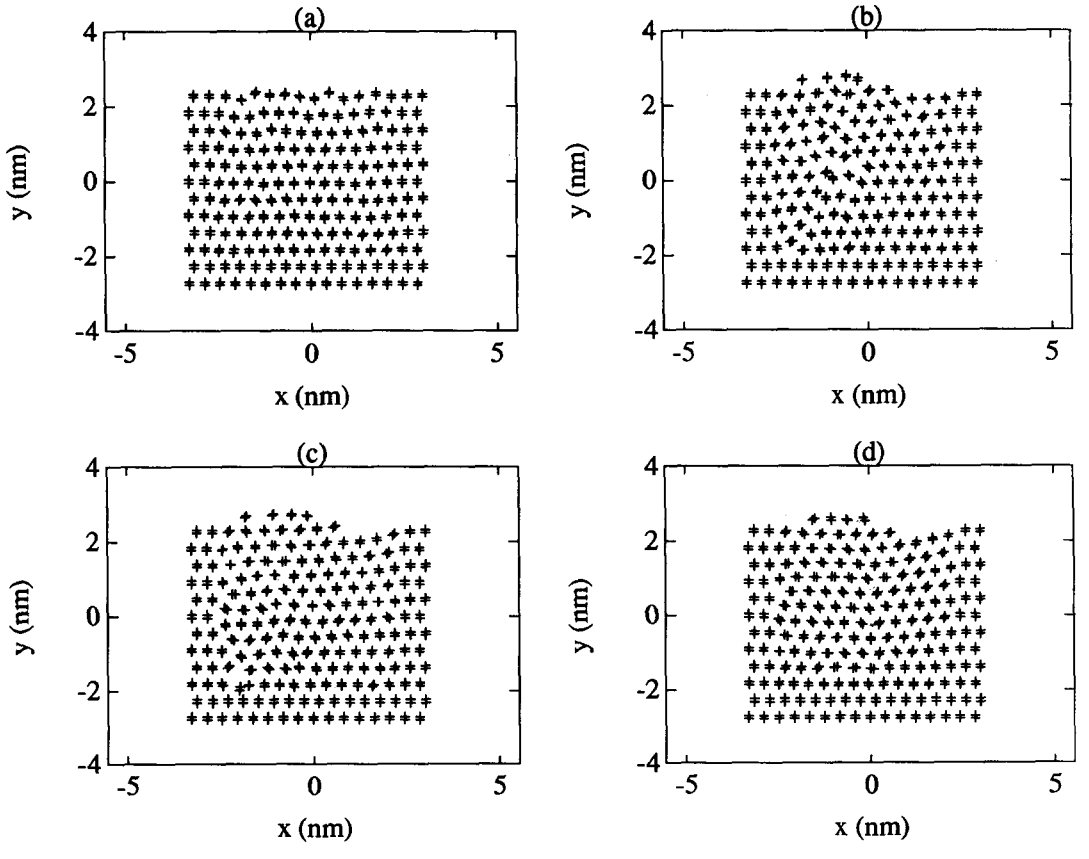

Figure 8 Averaged x–y projections of the crystal in simulation S11: (a) 2 ps, 440 K; (b) 10 ps, 400 K; (c) 23 ps, 272 K; (d) 70 ps, 297 K

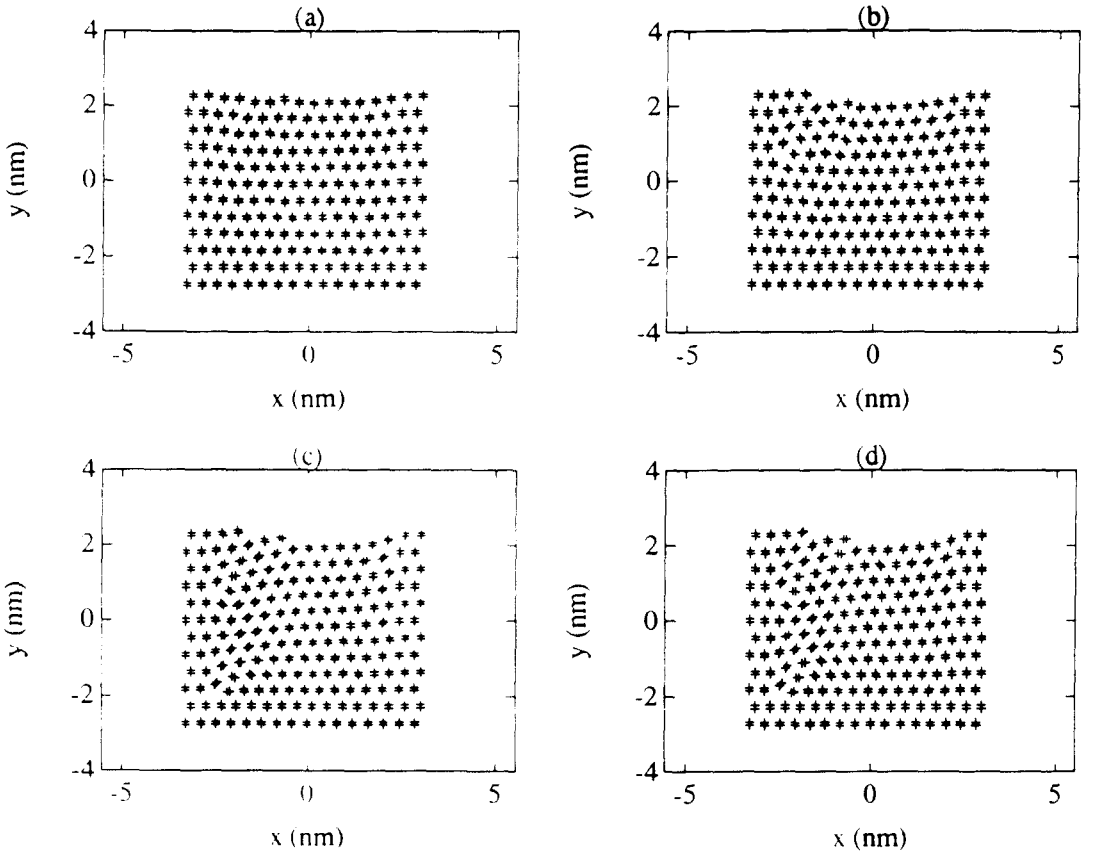

Figure 9 Averaged x–y projections of the crystal in simulation S12: (a) 11 ps, 237 K; (b) 14 ps, 223 K; (c) 60 ps, 172 K; (d) 100 ps, 144 K

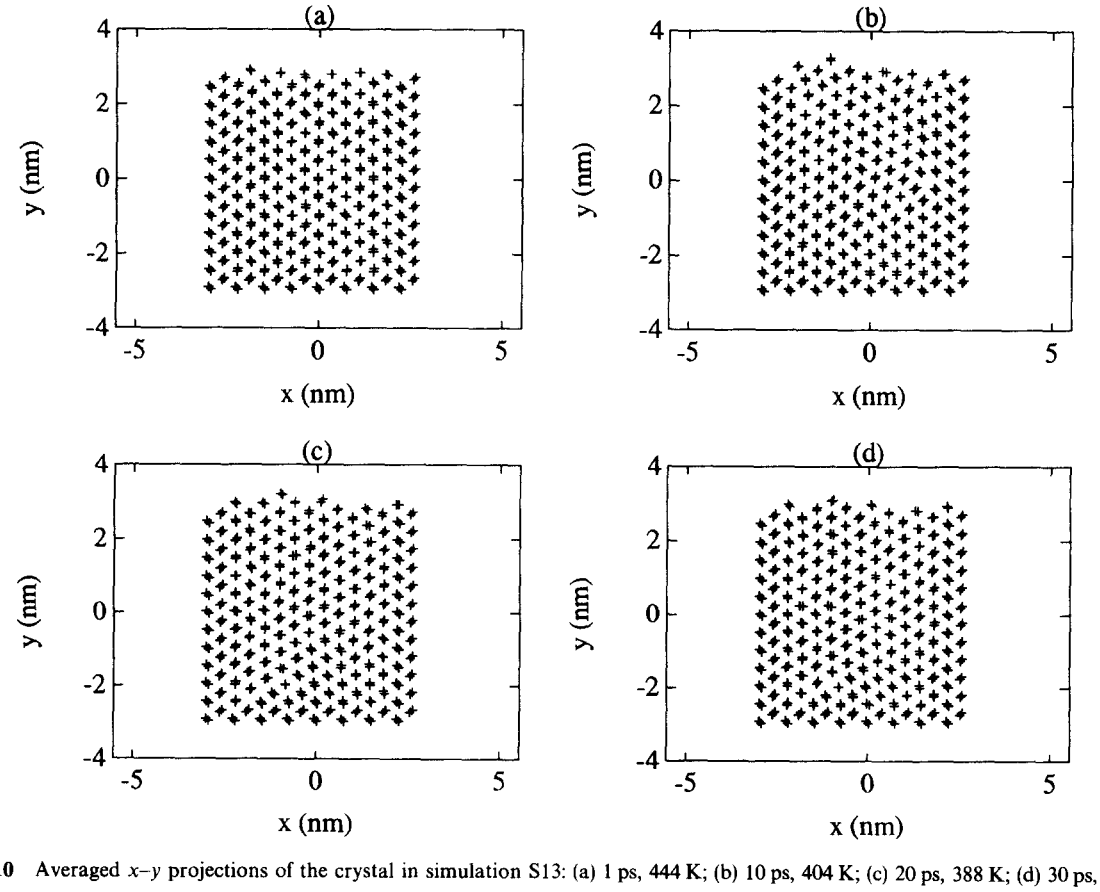

Figure 10 Averaged x–y projections of the crystal in simulation S13: (a) 1 ps, 444 K; (b) 10 ps, 404 K; (c) 20 ps, 388 K; (d) 30 ps, 362 K

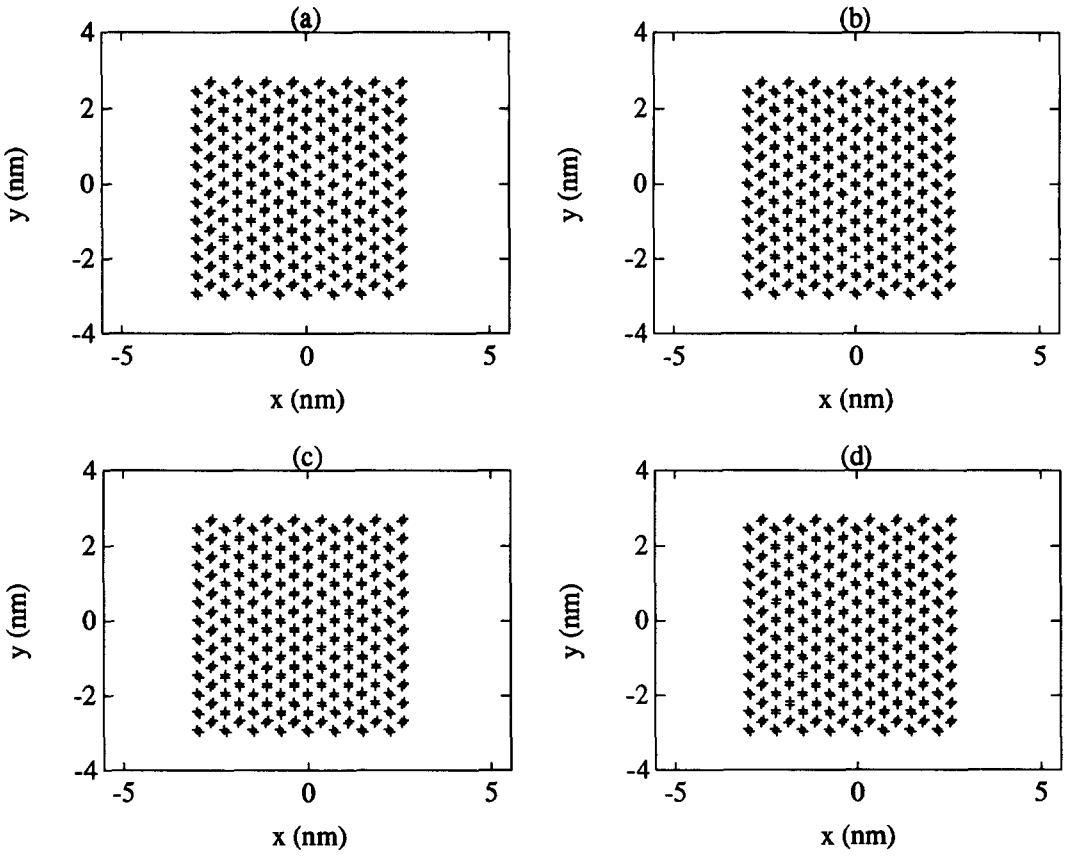

Figure 11 Averaged x–y projections of the crystal in simulation S14: (a) 2 ps, 333 K; (b) 20 ps, 301 K; (c) 50 ps, 246 K; (d) 66 ps, 225 K

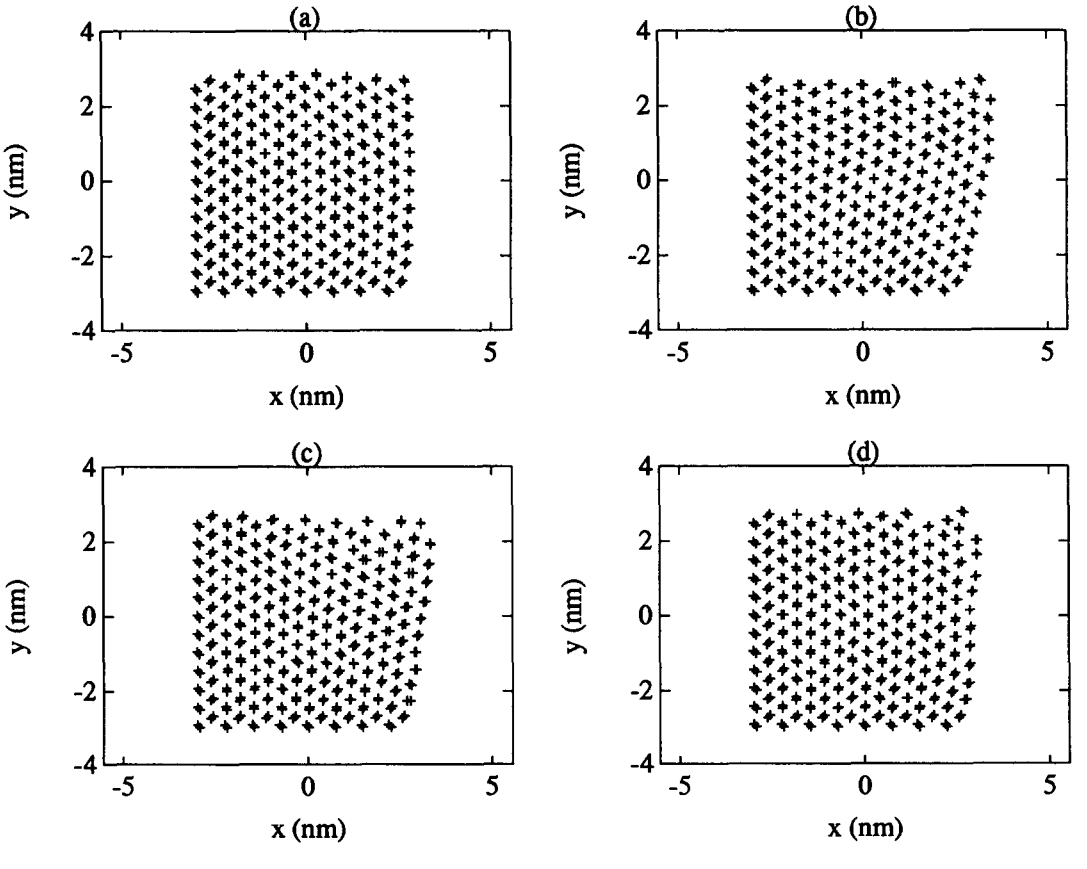

Figure 12 Averaged x–y projections of the crystal in simulation S15: (a) 1 ps, 423 K; (b) 5 ps, 392 K; (c) 10 ps, 394 K; (d) 15 ps, 379 K

more than 90° from the initial *trans* conformation. The concentration of *gauche* bonds was evaluated every picosecond for each crystal and plotted as a function of time, as shown in *Figure 13*. The temperature of the simulation was the main parameter govering the *gauche* concentration, in line with earlier work[23,24,29,39]. After a few picoseconds, a temperature-dependent steady state was reached. The distribution of *gauche* bonds in the crystal is given in *Figure 14*. It was found by marking the positions of the dynamic chains that contained at least one *gauche* bond at some time during the simulation. Unlike in the simulations of unconstrained crystals, where defects collected mainly at the surfaces[23–26] the *gauche* bonds are in the present case populating more of the inner chains of the crystal. The distribution of *gauche* bonds along the chain is shown in *Figure 15*. In the graphs, the numbers of *gauche* conformations observed during the total simulation were added. In all but the 4-SC crystal, the upper and lower chain-ends have the largest numbers of *gauche* bonds with a clear minimum in the centre. The 4-SC crystal of run S14 has less positional preference. The distribution of *gauche* bonds in run S10 is similar to that in S11.

Table 3 The lattice parameters of a 4-SC ORTH crystal (run S14 in *Table 2*) as a function of time

	a (nm)	*b* (nm)	*c* (nm)	α (deg)	β (deg)	γ (deg)	*t* (ps)
Maximum	0.6676	0.5430	0.2934	107.3	113.5	144.1	1
Minimum	0.3966	0.3698	0.2269	70.2	62.7	102.2	1
Mean	0.4940	0.4462	0.2583	89.7	90.0	123.4	1
STD[a]	0.0350	0.0257	0.0094	6.2	6.3	6.5	1
Maximum	0.6296	0.5881	0.2942	110.2	120.3	154.5	5
Minimum	0.3953	0.3737	0.2277	68.7	63.4	92.1	5
Mean	0.4939	0.4465	0.2586	90.3	89.5	123.4	5
STD	0.0317	0.0267	0.0090	6.2	6.3	6.2	5
Maximum	2.1115	2.1464	0.2914	111.6	115.2	169.8	10
Minimum	0.4082	0.3738	0.2284	65.0	68.6	19.8	10
Mean	0.4951	0.4477	0.2583	89.8	89.8	123.2	10
STD	0.0529	0.0527	0.0090	5.9	6.4	6.8	10
Maximum	0.6056	0.5540	0.2844	128.0	112.4	154.0	15
Minimum	0.3993	0.3760	0.2288	68.2	64.5	103.4	15
Mean	0.4927	0.4471	0.2565	89.7	89.6	123.3	15
STD	0.0305	0.0255	0.0087	6.3	6.2	5.9	15
Maximum	0.6307	0.5414	0.2871	113.8	113.1	114.4	20
Minimum	0.4128	0.3580	0.2309	61.1	68.8	101.2	20
Mean	0.4935	0.4468	0.2581	90.0	90.3	123.4	20
STD	0.0322	0.0253	0.0081	6.2	6.4	6.0	20

[a] Standard deviation from the mean value

Chain dynamics and mass transport

The diffusive motion of each dynamic chain was judged beyond the qualitative changes seen in *Figures 5–12* by the trajectory of its centre-of-mass coordinates (CMCs). The end-to-end distance (EED) of each dynamic chain was also calculated at every picosecond and was plotted as a function of time as an indicator of possible coiling of chain-ends or surface chains. We chose molecules that represented motion either on the surface of the crystal or in the middle for the different constraints. As concluded earlier, a rigid rotation of the whole chain is not likely[23,24].

Figures 16–18 give examples of CMC and EED plots for the high-temperature 3-SC MONO run S11.

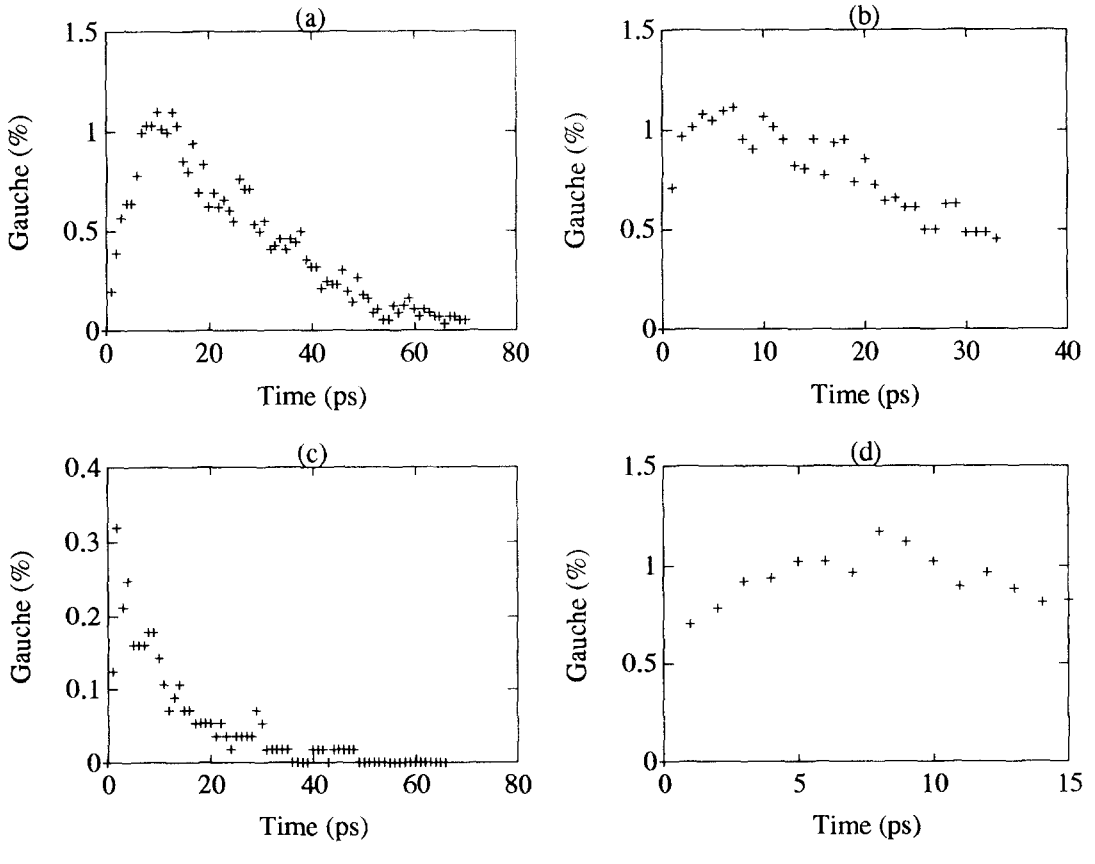

Figure 13 Concentration of *gauche* bonds as a function of time: (a) run S11; (b) run S13; (c) run S14; (d) run S15

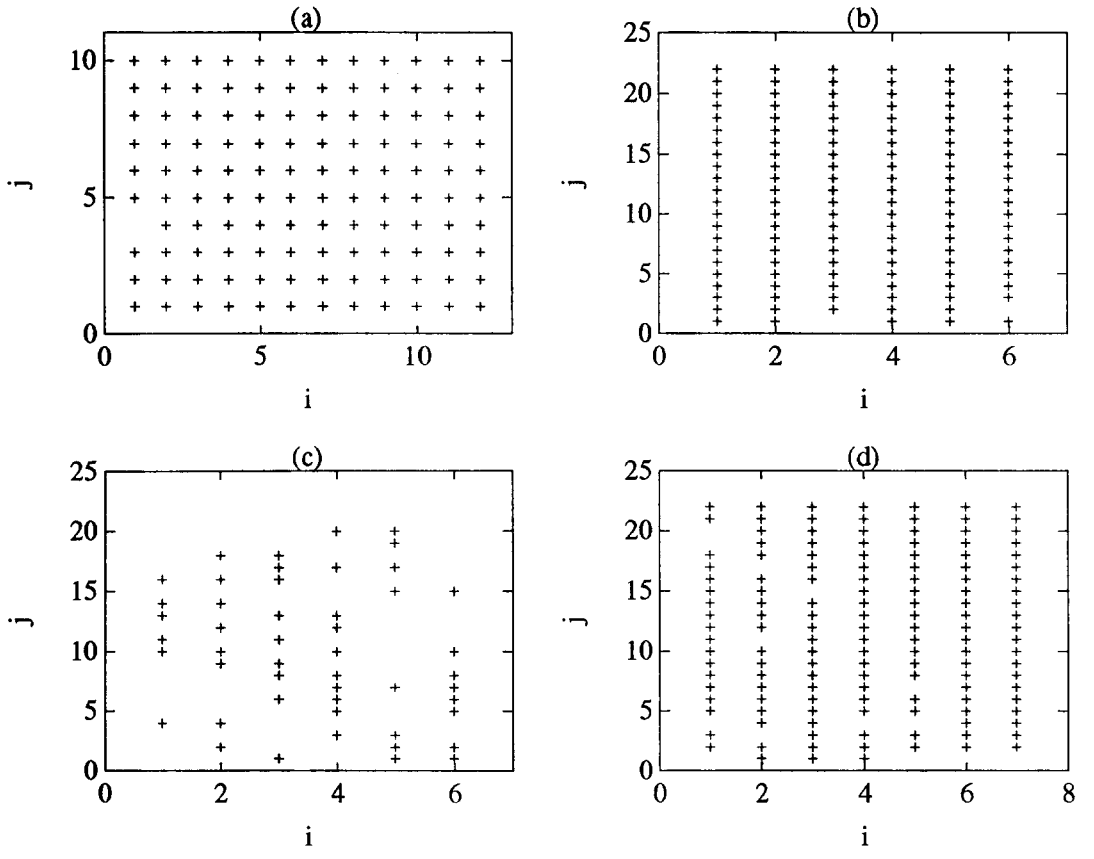

Figure 14 The positions of the dynamic chains (labelled with *i* and *j*) that contain *gauche* bonds: (a) rn S11; (b) run S13; (c) run S14; (d) run S15

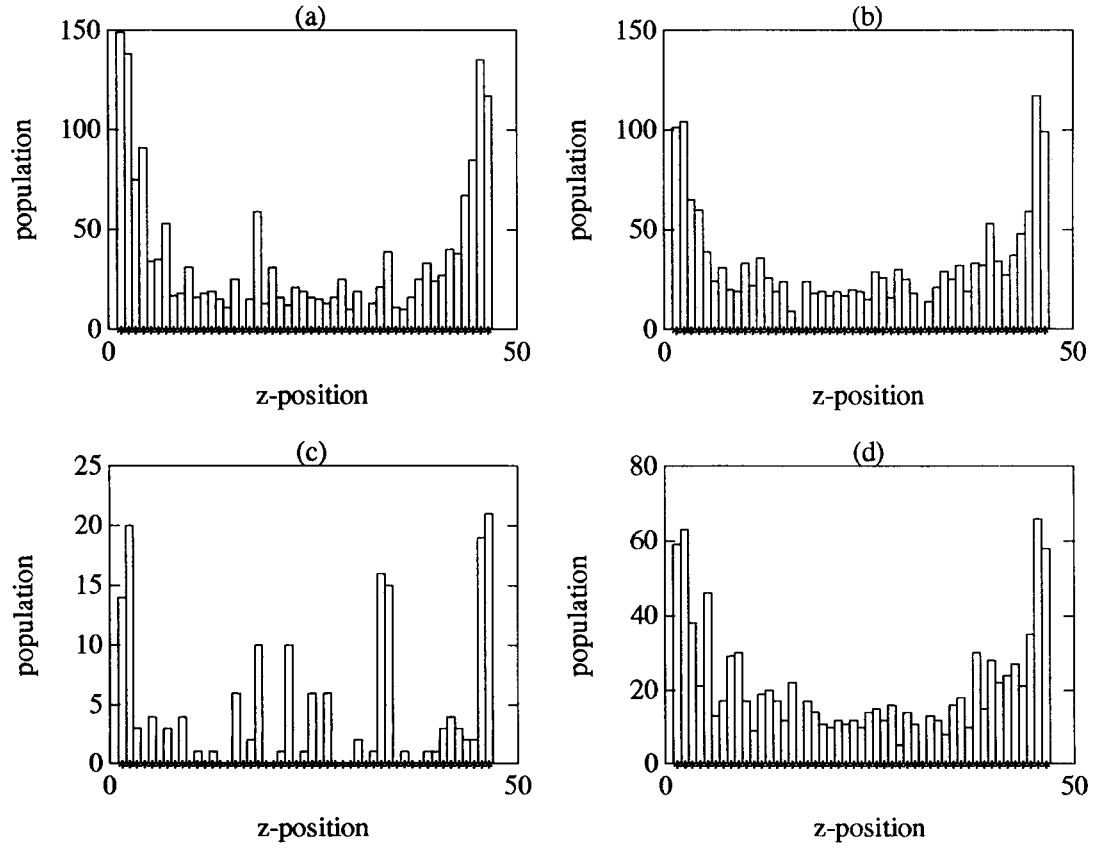

Figure 15 The distributions of *gauche* bonds along the *z*-axis: (a) run S11; (b) run S13; (c) run S14; (d) run S15

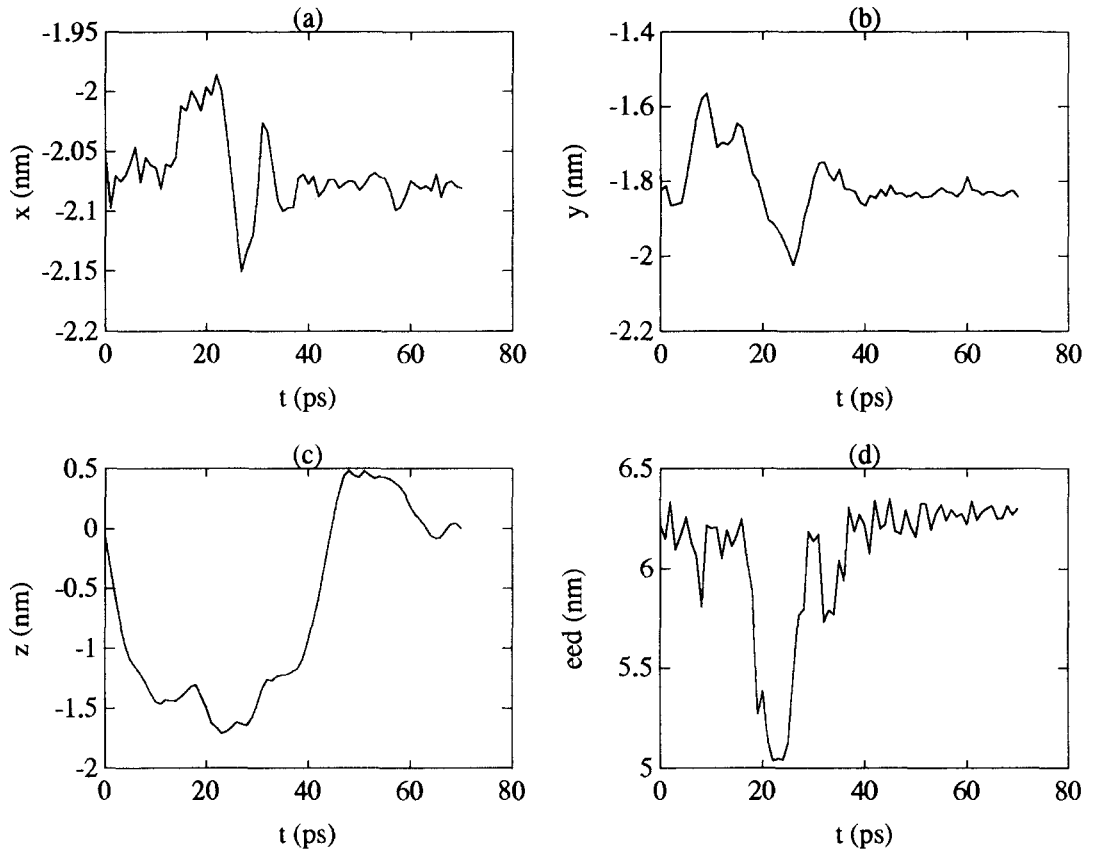

Figure 16 The trajectories of the centre-of-mass Cartesian coordinates (a–c) and the end-to-end distance (d) of the chain at the position $j=3$, $i=4$ in *Figure 1b* for the crystal of the simulation S11

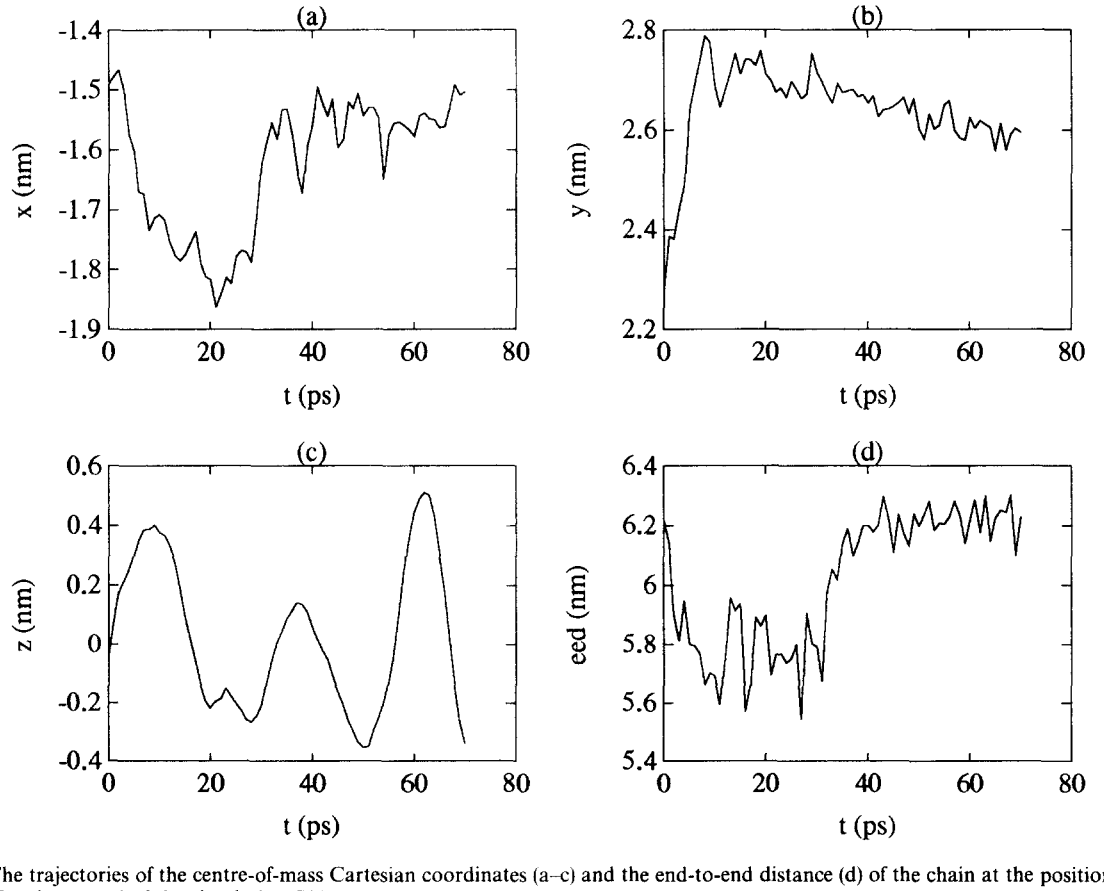

Figure 17 The trajectories of the centre-of-mass Cartesian coordinates (a–c) and the end-to-end distance (d) of the chain at the position $j=12$, $i=5$ in *Figure 1b* for the crystal of the simulation S11

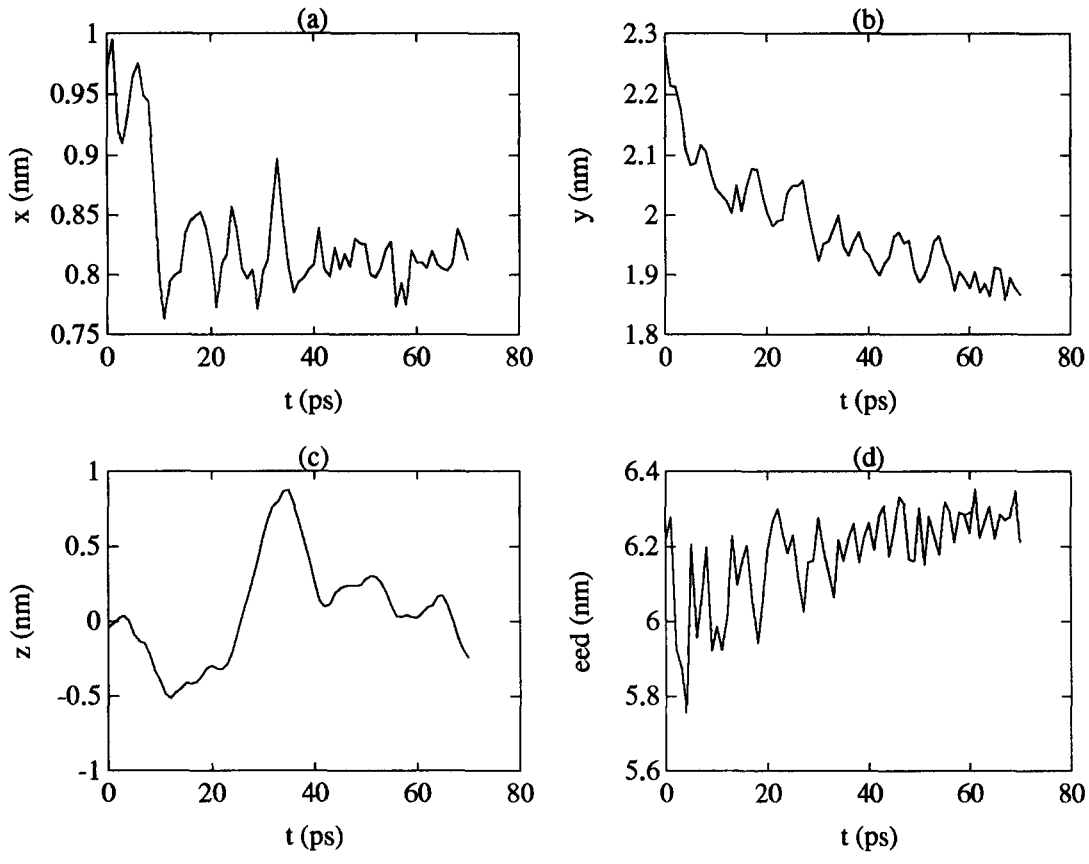

Figure 18 The trajectories of the centre-of-mass Cartesian coordinates (a–c) and the end-to-end distance (d) of the chain at the position $j=12$, $i=11$ in *Figure 1b* for the crystal of the simulation S11

Table 4 Times (t) and positions (k^a) of *gauche* bonds in the chain at $j=3$ and $i=4$ in simulation S11

t (ps)	8–11	13	14–19	20	27–29	33–34	35	36
k	11	7	2	10	8	2, 3	2	3

[a] Number of the CH_2 group in direction z counting from the bottom

Figure 16 shows the longitudional and transverse motions of the second dynamic chain at the lower-left inner position. The times and positions of the *gauche* bonds of this chain are listed in *Table 4*. *Figure 17* displays the third dynamic chain in the top layer from the left and *Figure 18* the third dynamic chain in the top layer from the right (see *Figures 1b*, *5* and *8*).

For the high-temperature 3-SC ORTH crystal of run S13, the disordering is lower, as can be seen by comparing *Figures 8* and *10*. The CMC and EED plots are given in *Figure 19* for the first dynamic chain in the upper-right corner (see *Figures 1a* and *10*). Its *gauche* bonds are detailed in *Table 5*.

When all the side surface chains are frozen (run S14), the chains can only have little lateral motion. Larger diffusion in the z direction becomes necessary to relieve the excess pressure caused by the constraint. The results are illustrated in *Figures 20* and *21* for mobile chains in the centre and in the upper-right corner, respectively (see *Figures 1a* and *11*).

The largest-scale diffusion was observed in run S15 where only two sides were fixed. *Figures 22* and *23* show this large motion for a chain in the upper-right third and the upper-right corner, respectively (see *Figures 1a*, *6* and *12*).

DISCUSSION

Energy, temperature and density

The simulations were initially designed to be at constant energy. The almost constant loss of 30–40 J mol^{-1} ps^{-1} of *Figure 2* arises from a technical limitation[25,26]. Owing to the truncation of the distance for non-bonded interaction at 1.0 nm (equation (5)), the local and global changes in atom positions lead to a continuous loss of energy whenever the neighbour list is changed. This energy loss is slow compared to the attainment of the steady-state temperature. The latter takes less than 5 ps (see *Figure 3*). One can thus make use of the unintended energy loss to study the effect of cooling (at a rate of about 2 K ps^{-1}).

One of the temperature-sensitive properties is the density of the crystal, as shown in *Figure 4*. The simulation time can be related to temperature by comparison to *Figure 3*. For crystals of partial constraint of the sides (*Figures 4a*, *4b* and *4d*) there is an adjustment of the density of the crystal within about 4 ps. The MONO (*Figure 4a*) and ORTH (*Figures 4b* and *4d*) crystals behave somewhat differently in their approach to steady state. Beyond about 25 ps, a regular increase in density occurs, paralleling the temperature decrease. The experimental increase in density is about 0.025 g cm^{-3} per 100 K^1, close to the change that can be deduced from *Figure 4a*. The irregularities between 5 and 25 ps seem to be related to

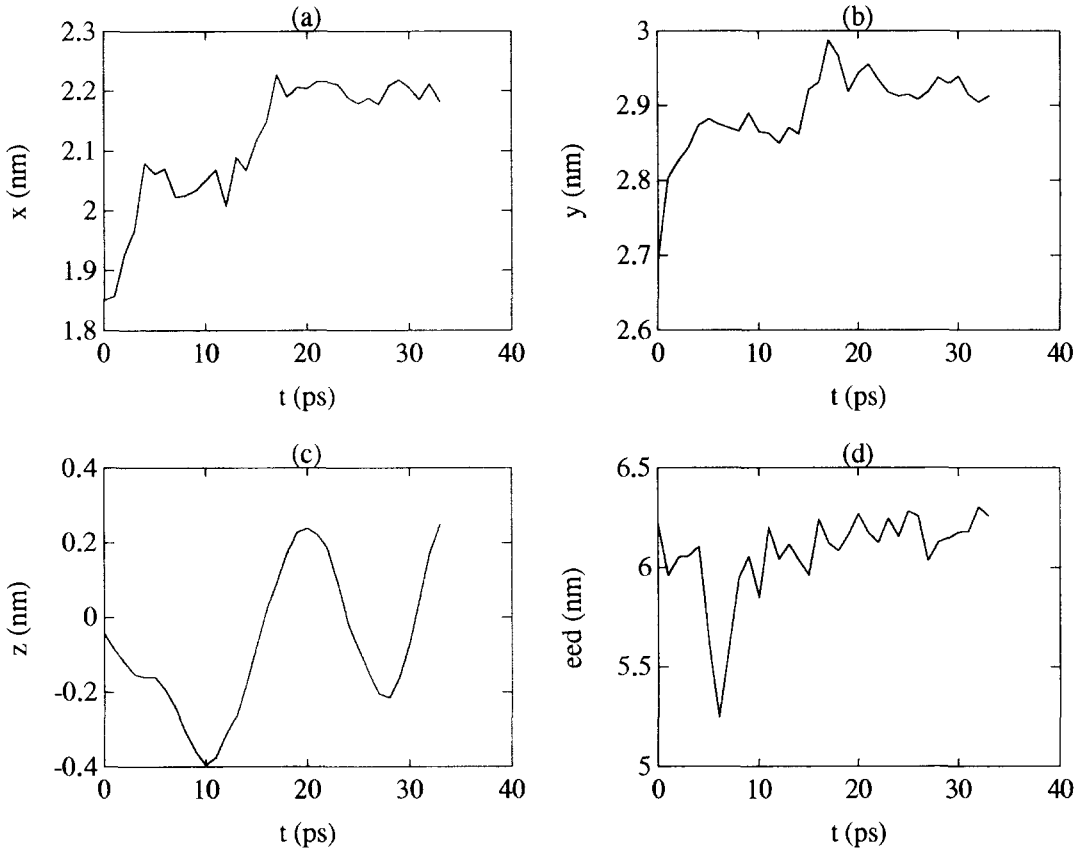

Figure 19 The trajectories of the centre-of-mass Cartesian coordinates (a–c) and the end-to-end distance (d) of the chain at the position $j=24$, $i=7$ in *Figure 1a* for the crystal of the simulation S13

Table 5 Times (t) and positions (k^a) of *gauche* bonds in the chain at $j=22$ and $i=6$ in simulation S13

t (ps)	1	2	3	4	5	6	8	9	10	12
k	45	45	22, 24	22, 24	26	3	11, 18	19, 35	23, 26	8, 23
t (ps)	13	14	15	16	17	18	19	22	27	
k	8, 19	45	40	32, 40	32, 43	43	1	3	45	

[a] Number of the CH_2 group in direction z counting from the bottom

the defect generation and mass transport connected with plastic flow, as well as the beginning of melting. The experimental melting temperature of pentacontane, the equivalent paraffin, is 365 K. Simulations of the melting of unconstrained and constrained crystals were discussed earlier and showed fast internal disordering followed by slower surface melting[25,26].

For the fully side-constrained crystal (run S14, 4-SC, *Figure 4c*), the decrease in temperature cannot change the interior density. Only in the upper and lower parts of the crystal is the density lower because of chains having partially moved out of the crystal (see *Figure 7*). The amplitude of the density fluctuations is for this case quite regular and decreases with decreasing temperature. All four simulations show a surprisingly regular volume-breathing mode of vibration with a temperature-independent frequency of about 1.0×10^{12} Hz.

Structure changes

Without constraint, the earlier UA simulations always led to hexagonal crystal structures with equal a and b single-atom unit cell parameters[23–26]. This hexagonal structure consisted of dynamic, nanometre-sized domains of locally parallel zigzag chains changing in rotation angle via a twist motion coupled to the breathing mode of the crystal[24]. From the present simulations of constrained crystals, represented by the averages in *Figures 5*, *6* and *8–12*, it is clear that the steady-state structure of the dynamic chains is not hexagonal. The ratio of the a and b parameters of the constraining surfaces is largely retained. This is particularly true for the four-sided constraint of the ORTH run S14 (see *Table 3* and *Figure 11*), but also the MONO and the less fully constrained ORTH crystals show a continuation of the surface chain spacings into the interior of the dynamic chains up to the fault areas. The MONO crystals S10–S12 thus remain monoclinic outside of the fault areas. Inspection of *Figures 10–12* reveals that the ORTH crystals lose their 90° herring-bone setting angle of the zigzag chains (see *Figure 1a*). Parallel packing of the zigzag chains is preferred and achieved within 1 ps (see *Figures 10a* and *11a*). The low-temperature crystal with four-sided constraint (*Figure 11d*) shows an almost perfect crystal with all dynamic chains parallel with a setting angle of 90°, intermediate to the two ORTH orientations.

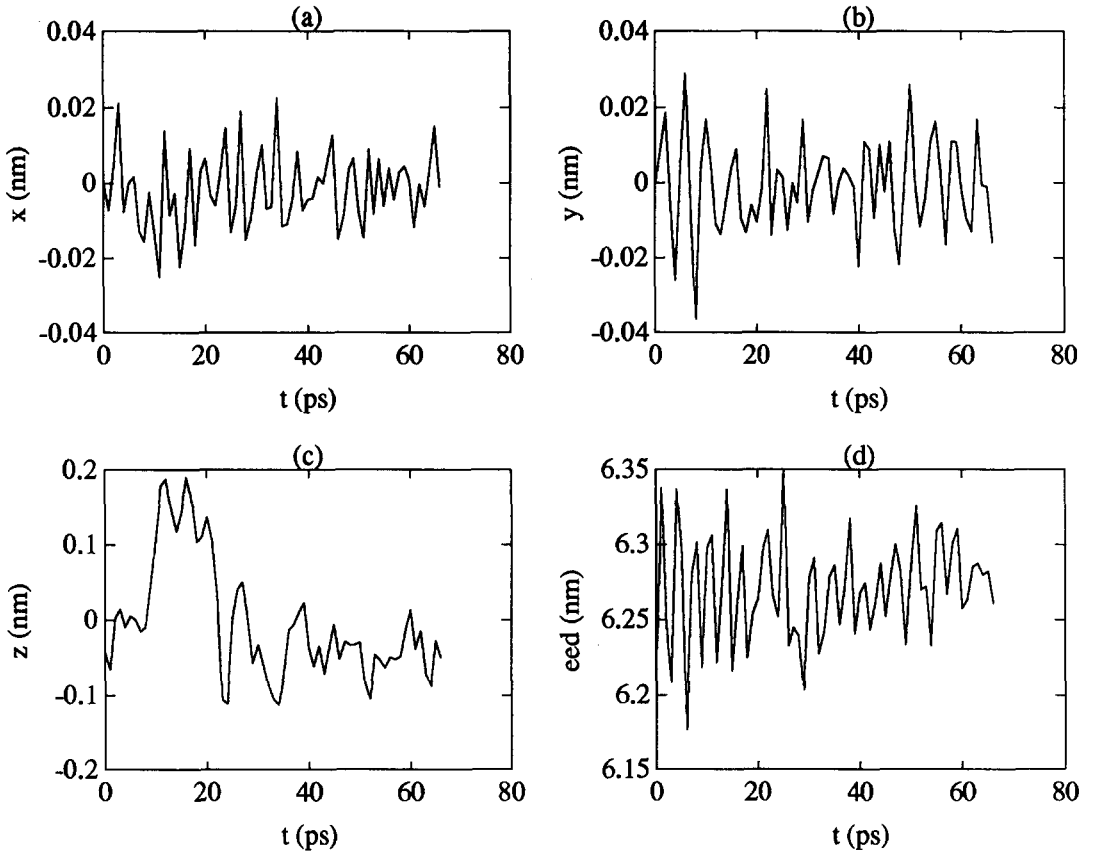

Figure 20 The trajectories of the centre-of-mass Cartesian coordinates (a–c) and the end-to-end distance (d) of the chain at the position $j=13$, $i=5$ in *Figure 1a* for the crystal of the simulation S14

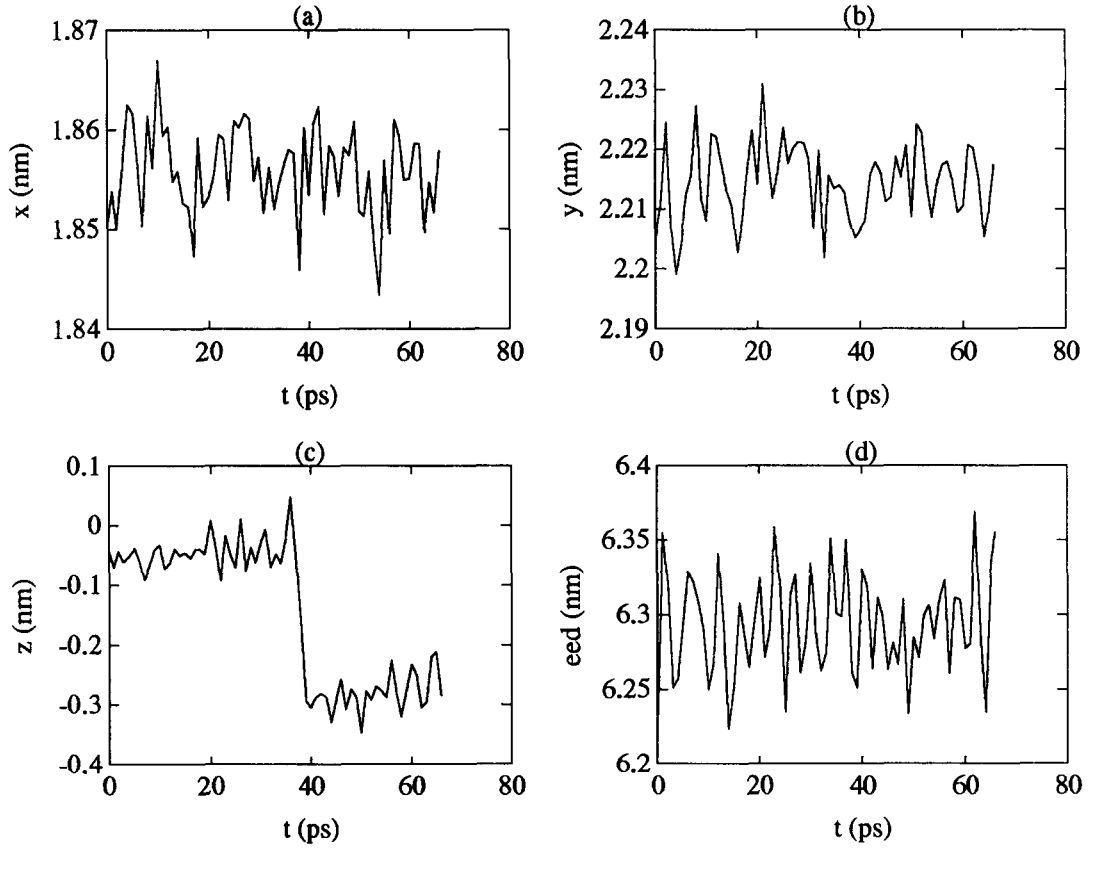

Figure 21 The trajectories of the centre-of-mass Cartesian coordinates (a–c) and the end-to-end distance (d) of the chain at the position $j=22$, $i=7$ in *Figure 1a* for the crystal of the simulation S14

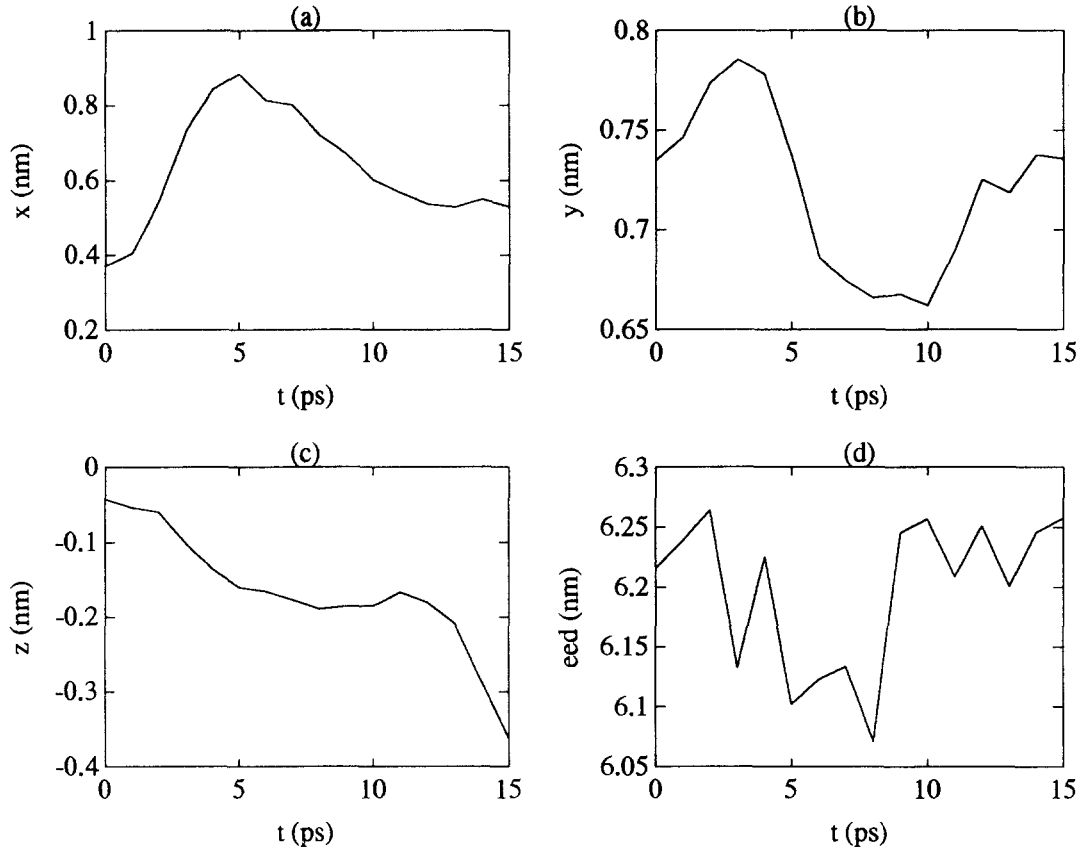

Figure 22 The trajectories of the centre-of-mass Cartesian coordinates (a–c) and the end-to-end distance (d) of the chain at the position $j=16$, $i=5$ in *Figure 1a* for the crystal of the simulation S15

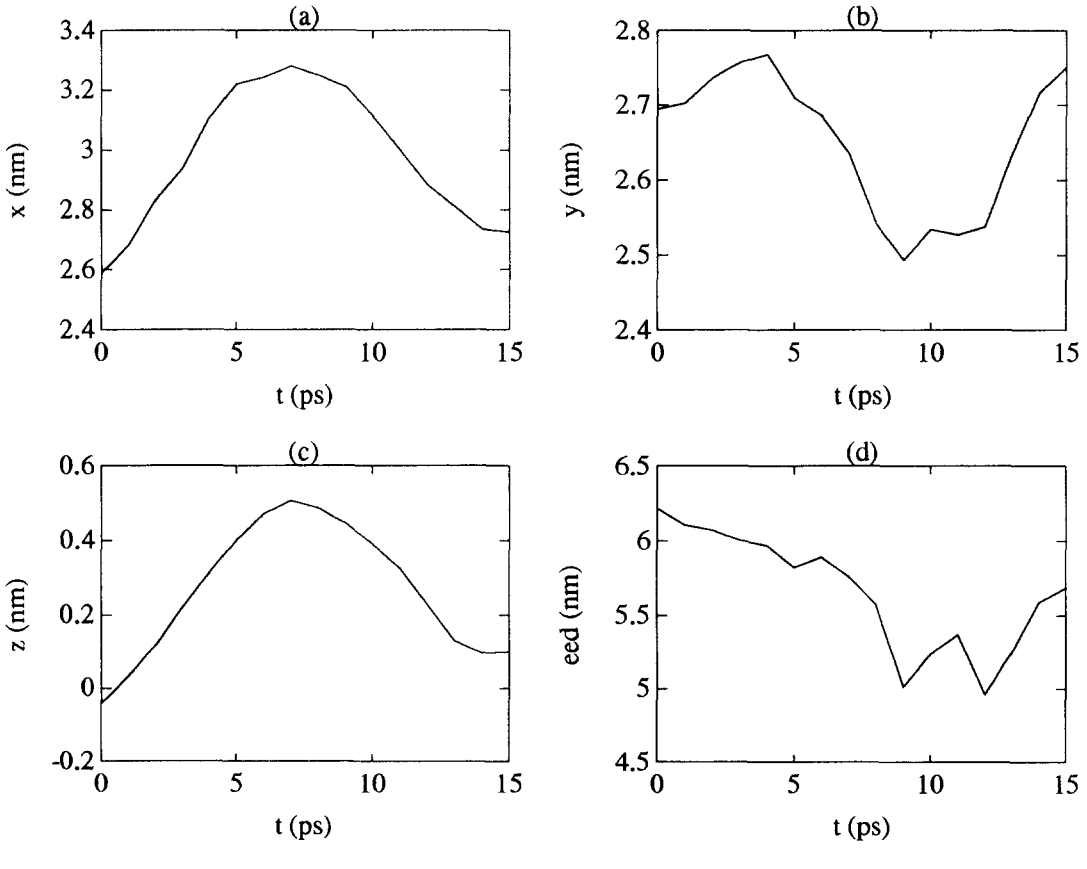

Figure 23 The trajectories of the centre-of-mass Cartesian coordinates (a–c) and the end-to-end distance (d) of the chain at the position $j=24$, $i=8$ in *Figure 1a* for the crystal of the simulation S15

The reason for the absence of a dynamic twisting of the chains may well be the lack of an appropriate lattice vibration mode to produce the cooperative setting angle changes. The reason for the absence of a clear domain structure may rest with the smaller sizes of the dynamic aggregates and the presence of the constraint. *Figures 5* and *6* show, perhaps, a beginning of domain formation close to the free surfaces.

Conformational analysis

With the earlier molecular dynamics simulations we were able to gain information on the concentration, distribution and lifetime of *gauche* defects and their role in mass transport[22–24,29,39]. The main observation was that the formation of *gauche* defects and kinks needed the concerted action of torsional, longitudinal and transverse skeletal vibrations[29]. The *gauche* concentrations of *Figure 13* show a quick rise to a steady state followed by a decrease, in accord with the decrease in temperature. In the partially constrained crystals a maximum in *gauche* concentration is reached between 5 and 10 ps. The lifetimes of the *gauche* bonds vary but are, depending somewhat on position, between 1 and 3 ps, with rare extensions as long as 10 ps.

The distribution of *gauche* bonds in the crystal changes with the constraint. In unconstrained crystals, most of the *gauche* bonds were found at the surface or next to it and at the chain-ends[23–26]. Only a few *gauche* bonds were found in the interior of the crystal. In the constrained crystals all chains develop *gauche* defects at some time, as shown in *Figure 14* (see *Figures 1a* and *1b* to locate the chains), and the interior chains also have some *gauche* conformations towards their middles, as shown in *Figure 15*.

The reason for this dependence of the location of *gauche* defects is not known. One may speculate, however, that changes in crystal and domain size and constraint change the skeletal vibrational modes of these small-volume elements sufficiently to affect the location favourable for *gauche* bond formation. A similar suggestion was made above as an explanation for the reduction in the formation of domains with dynamic setting angles in constrained crystals. Considering the volume-breathing mode, one should note that the fundamental vibration should have its nodes at the surface when constrained and in the centre when unconstrained.

There also exists a discrepancy in the i.r. measurements of *gauche* defects using normal mode analysis to characterize the conformational defects from the spectra measured for selectively deuterated samples. Zerbi *et al.*[42] found that practically all *gauche* bonds of their sample were at the chain-ends, while Snyder *et al.*[43] (using the same force field[44] for computation) found that *gauche* bonds can also exist in the middle of the chain. The concentration of the *gauche* bonds increases in the latter case exponentially towards the chain-ends, as was also seen in *Figures 15a*, *15b* and *15d*. Perhaps this difference is not only because of differences in sensitivity of the analyses but also in the types of crystals analysed. The results of Zerbi *et al.* agree with our unconstrained simulations, and the results of Snyder *et al.* are similar to our constrained simulations.

Chain dynamics and mass transport

In all high-temperature simulations the crystals must expand out of their constraints because the initial coordinates were taken from the room-temperature lattice dimensions. An estimation of the initial hydrostatic pressure in a fully side-constrained crystal can be based on the experimental compressibility of ORTH polyethylene (2.67×10^{-10} Pa^{-1})[45], the density of a simulated unconstrained crystal (at about 400 K, 0.96 g cm^{-3})[23] and the initial density estimated by the same box-sampling method (1.02 g cm^{-3}). These data result in an instantaneous hydrostatic pressure of about 500 MPa (5000 times atmospheric pressure). This high initial pressure is the main reason for the mass transport in the high-temperature simulations. In comparison, the incipient melting is a minor effect because only surface chains start to disorder in the short time of the simulation[25,26].

In the 3-SC simulation of a MONO crystal (run S11) illustrated in *Figures 5* and *8*, the initial disordering can be seen after 2 ps as a buckling of the surface layers. The defects propagate inwards, producing an overall outward (lateral) mass transport. At 10 ps (*Figure 8b*), some disorder has reached the innermost layer in the lower left of the crystal, producing a fault line parallel to (201). Along the fault line, the (001) layers are buckled, or can be considered as containing a series of edge dislocations of opposite Burgers vectors ($j=3$, 4 and 9, 11; for numbering see *Figure 1a*)[1]. Four of the upper-left surface chains have been squeezed out into a new top layer ($j=13$), while the old top surface layer ($j=12$) has been shortened from 16 to nine chains. Layer $j=11$ connects on the right to $j=12$, i.e. there must be an extra layer somewhere in the crystal, ending in an unpaired edge dislocation. This layer is $j=8$ (on the right, with only eight chains in the layer). Counting across the buckled chains, the numbers of chains per (001) layer are then (counting on the left with decreasing j and starting with $j=12$) 9, 15, 14, 15, 15 (extra layer of eight, $j=8$ on the right), 16, 16, 16, 16 and 16. After 23 ps (*Figure 8c*), the buckles along the (201) fault have decreased in severity and the reduction in density has reached the bottom of the crystal. The layer density sequence is now (counting as before) 9, 15, 14, 15, 14 (extra layer of 13, $j=8$ on the right), 15, 15, 15, 15 and 16. The edge dislocation at $j=8$ has absorbed the extra chains from the inner layers and grown across the crystal (to 13 chains). At 70 ps (*Figure 8d*), the temperature has dropped to room temperature (297 K), removing the initial pressure. The dynamic chains in the inner layers have started to perfect, both in position and setting angles. The layer density and the edge dislocation have, however, changed only little. The four expelled chains do not regain a stable position but remain incomplete, along with layer $j=12$ (left). Even after 100 ps (at 255 K, see *Figure 5d*) the structure has not changed significantly. By now the equilibrium density is higher than provided by the rigid frame, but the number density of the layers is not increased, the lower volume being accommodated by a stronger downward curvature of each layer.

Figures 16–18 show the CMC and EED plots of three strategic chains of the simulation S11. *Figure 16* illustrates the chain j, $i=3$, *4* at the lowest-left buckle (or between the $j=3$ and 4 dislocation pair of *Figure 8b*). The chain first moves upwards, approximately in the direction of

the fault line (201) (0.2 unit cell length in direction x and 0.4 in y), creating a void that relieves the pressure in the interior of the crystal. By the end of the simulation (at room temperature) it has moved back to a position of almost perfect order (at 70 ps, *Figure 8d*). During this excursion, the chain slides temporarily out of the crystal by up to six unit cell lengths or 12 CH_2 units (between 0 and 40 ps, see *Figure 16c*). The EED shows a shortening of the chain at about 23 ps (with little help from *gauche* bonds, see *Table 4*). This bending of the chain-end may well have moved the CMC in the opposite direction (*Figure 8c*). The fastest speed of the longitudinal motion is about 200 m s^{-1}, i.e. less than 10% of the speed of sound[24]. As observed earlier, the longitudional motion of a chain out of the crystal is coupled to the longitudinal acoustic mode and enhanced by the presence of *gauche* defects[29]. After 40 ps all *gauche* bonds have disappeared (see *Table 4*) and only the normal change of the EED because of the longitudinal acoustic mode (LAM, $\approx 4 \times 10^{11}$ Hz) remains. No kinks, i.e. *gauche-trans-gauche* sequences, were found during the motion of the chain, and, as suggested before, no mechanism including kink propagation was observed[25,26,36].

Figures 17 and *18* refer to surface chains at positions $i=5$ and 11, respectively, i.e. they are chains involved in the break-up of the top layer. The chain $i=5$ has popped up to layer $j=13$ after 10 ps and continues moving left for 20 ps to reach approximately position $i=4$ and moves up and down by as much as one unit cell length in z. The other three chains of the new layer $j=13$ came from positions 6, 7 and 8 of layer $j=12$. The shrinkage of the dynamic section of the crystal with decreasing temperature can be seen from *Figure 17b*. The chain $i=11$ moves to the right by 20% of the unit cell length and down by 80% to connect to layer $j=11$. Somewhat further excursions occur in the z direction (3.5 unit cell distances).

In the low-temperature simulation (*Figure 9*), disordering and lateral mass transport are also observed; however, the crystal shrinks into the rigid enclosure instead of expanding. After 11 ps the surface layer shows an inward curvature and a buckling on the left. After 14 ps (*Figure 9b*, 223 K), the right part of the crystal has slipped into the constraint (along a (201) slip plane), producing an edge dislocation at position $j=9$ on the right (13 chains). Below the dislocation, all layers still have 16 chains; above, 4, 16, 15 and 16*. After 60 ps (*Figure 9c*), the temperature has further dropped to 172 K and a second slip along a parallel slip plane has occurred, giving a second edge dislocation at position $j=3$. The layer density of the chains has equalized throughout the crystal, alternating between 16 and 15. Except for better order and larger curvature, little has changed at the end of the simulation (100 ps, 144 K, *Figure 9d*).

The crystals with initially an ORTH structure show a somewhat different expansion mechanism (*Figure 10*, 3-SC, S13, 457 K; compare with MONO S11, *Figure 8*). The most densely packed planes are now of the form {110}, the diagonals in the figures. In the first frame, after 1 ps, the setting angle has changed, as discussed above, and the top six layers ($j=19$–24) have uniformly expanded into the open space. After 10 ps (*Figure 10b*), a dislocation appears (at the end of the (110) plane going through the lower-left corner), but the bottom layers up to $j=6$ remain approximately in their original positions and the free surface becomes disordered. In the last two frames, a steady state seems to have been reached with the dislocation having moved to the position $i, j=4, 5$ at the bottom (the extra layer is now $(\bar{1}10)$). A total of about six chains have been removed from the initial volume, in contrast to only four in the MONO crystal for a similar time and temperature.

The movement of the upper-right dynamic chain is depicted in *Figure 19*. The quick initial expansion in direction y is about one quarter of a unit cell (1 ps) and increases more slowly to about half a unit cell. The slower movement is coupled with motion in the x direction by half a unit cell, placing the chain ultimately into the neighbouring crystal position on the (110) plane. Being a surface chain, it shows considerable conformational disorder (see *Table 5*), including kink formation.

Figure 11 depicts the changes for the 4-SC structure. As expected, practically no defects can be seen in the x–y projections of the averages of the chains. All mass transport had to occur by longitudinal diffusion along z. *Figure 7* illustrates the results after 10 ps. The chains in contact with the rigid support show the least disorder, as expected, but contribute also to the longitudinal mass transport.

Figures 20 and *21* show the motions of chains in the centre and the upper-right corner. The magnitudes of the motions are, as expected, considerably smaller. The centre chain moves between 10 and 20 ps for about one unit cell (one zigzag) out of the crystal (*Figure 20c*) without effect on the other motion indicators except for the disturbance in the LAM (*Figure 20d*). Similarly, the unit cell jump of the centre chain at about 35 ps gives a change in the LAM in *Figure 21d*.

The results from the simulation of a dynamic crystal placed into a rigid corner (*Figure 12*, 2-SC, S15) show that the expansion of the ORTH crystal occurs with some preference for the x direction. Both *Figures 11* and *12* indicate that the x dimension is too small for the initial ORTH packing of the UA chains and is adjusted quickly by chain rotation and, if permitted, lateral diffusion. This observation is consistent with earlier simulations using unconstrained ORTH crystals[23–26]. The first step is again a fast expansion beyond the initial crystal dimensions and rotation of the chains to a 90° setting angle. All of the extra volume needed at the higher temperature is generated by this outward expansion and a curvature of the {110} planes. *Figure 6* illustrates also the fusion with the beginning of surface melting at about 6 ps.

Figures 22 and *23* document the motions of a chain in the middle ($i=5$), about two-thirds up the crystal ($j=16$), and the upper-right corner, respectively. The regular transverse vibrations are missing for these two chains. The large-amplitude motion is now a continuous flow, except for the LAM that still exists at approximately the old frequency.

CONCLUSIONS

The molecular dynamics simulations of surface-constrained crystals provide new information on density changes, structure, defects and mass transport. Similar to the

* The reason for the decrease in layer density, despite an overall density increase, is an increase of the simulated MONO crystal in the x direction which is more than compensated for by a decrease in y. This change in lattice parameters was shown before to be linked to a different packing of the UA CH_2 groups[24]

unconstrained simulations, structural change, molecular motion and the lifetime of *gauche* defects are on a picosecond time-scale[39]. The constraints suppress for the chosen crystal size the earlier-observed domain formation[24] and give different *gauche* bond distributions. Mass transport is the result of coupling among different modes of skeletal vibration. The internal pressure is in the present simulations the main driving force for mass transport. The observed lateral mass transport provides an initial mechanism for plastic deformation of the crystals involving affine expansion and contraction, development of crystallographic fault lines (slip planes), edge dislocations and curved lattice planes. The longitudinal mass transport follows the earlier-established mechanism involving stationary conformational defects and motion driven by skeletal vibrations[29].

ACKNOWLEDGEMENTS

This work was supported by the Division of Materials Sciences, Office of Basic Energy Sciences, US Department of Energy under contract DE-AC05-84OR21400 with Martin Marietta Energy Systems Inc., and the Division of Materials Research, National Science Foundation, Polymers Program under grant DMR 92-00520.

The Chancellor of The University of Tennessee and the University Computing Center are acknowledged for providing computing facilities and services.

REFERENCES

1 Wunderlich, B. 'Macromolecular Physics', Vols 1–3, Academic Press, New York, 1973, 1976, 1980
2 Müller, A. and Saville, W. B. *J. Chem. Soc.* 1925, **127**, 599
3 Müller, A. *Proc. R. Soc. London, Ser. A* 1932, **138**, 514
4 Kim, Y., Strauss, H. L. and Snyder, R. G. *J. Phys. Chem. 1989,* **93**, 7520
5 Olf, H. and Peterlin, A. *J. Polym. Sci. A-2* 1970, **8**, 791
6 Strobl, G., Ewen, B., Fischer, E. W. and Piesczek, W. *J. Chem. Phys.* 1974, **61**, 5257
7 Ewen, B., Fischer, E. W., Piesczek, W. and Strobl, G. *J. Chem. Phys.* 1974, **61**, 5265
8 Ewen, B., Strobl, G. R. and Richter, D. *Faraday Discuss. Chem. Soc.* 1980, **69**, 19
9 Ewen, B. and Richter, D. *J. Chem. Phys.* 1978, **69**, 2954
10 Doucet, J. and Dianoux, A. J. *J. Chem. Phys.* 1984, **81**, 5043
11 Guillaume, F., Doucet, J., Sourisseau, C. and Dianoux, A. J. *J. Chem. Phys.* 1989, **91**, 2555
12 Ungar, G. *J. Phys. Chem.* 1983, **87**, 689
13 Ungar, G. and Masic, N. *J. Phys. Chem.* 1985, **89**, 1036
14 Ungar, G. *Macromolecules* 1986, **19**, 1317
15 Yamamoto, T. *J. Chem. Phys.* 1985, **82**, 3791
16 Yamamoto, T. *J. Chem. Phys.* 1988, **89**, 2356
17 Ryckaert, J.-P., McDonald, I. R. and Klein, M. L. *Mol. Phys.* 1989, **67**, 957
18 Ryckaert, J.-P. and Klein, M. L. *J. Chem. Phys.* 1986, **85**, 1613
19 Pechhold, W., Blasenbrey, S. and Woerner, S. *Kolloid Z. Z. Polym.* 1963, **189**, 14
20 Reneker, D. H. and Mazur, J. *Polymer* 1988, **29**, 3
21 Mansfield, M. and Boyd, R. H. *J. Polym. Sci., Polym. Phys. Edn* 1978, **16**, 1227
22 Sumpter, B. G., Noid, D. W., Liang, G. L. and Wunderlich, B. *Adv. Polym. Sci.* 1994, **116**, 27
23 Liang, G. L., Noid, D. W., Sumpter, B. G. and Wunderlich, B. *Makromol. Chem., Theory Simul.* 1993, **2**, 245
24 Liang, G. L., Noid, D. W., Sumpter, B. G. and Wunderlich, B. *J. Polym. Sci., Polym. Phys. Edn* 1993, **31**, 1909
25 Liang, G. L., Noid, D. W., Sumpter, B. G. and Wunderlich, B. *Acta Polym.* 1993, **44**, 219
26 Wunderlich, B., Liang, G. L., Noid, D. W. and Sumpter, B. G. in 'Proc. MRS Meeting', Vol. 321, MRS, Pittsburgh, PA, 1994
27 Liang, G. L., Noid, D. W., Sumpter, B. G. and Wunderlich, B. *Compos. Polym. Sci.* 1993, **3**, 101
28 Wunderlich, B. *Faraday Discuss. Chem. Soc.* 1979, **68**, 239
29 Sumpter, B. G., Noid, D. W. and Wunderlich, B. *Macromolecules* 1992, **25**, 7247
30 Bunn, C. W. *Trans. Faraday Soc.* 1939, **35**, 482
31 Seto, T., Hara, T. and Tanaka, K. *Jpn. J. Appl. Phys.* 1968, **7**, 31
32 Wool, R. P., Bretzlaff, R. S., Li, B. Y., Wang, C. H. and Boyd, R. H. *J. Polym. Sci. B* 1986, **24**, 1039
33 Brown, D. and Clarke, J. H. R. *J. Chem. Phys.* 1986, **84**, 2858
34 Boyd, R. H. and Breitling, S. M. *Macromolecules* 1974, **7**, 855
35 Sorensen, R. A., Liam, W. B. and Boyd, R. H. *Macromolecules* 1988, **21**, 194
36 Neusy, E., Nosé, S. and Klein, M. L. *Mol. Phys.* 1984, **52**, 269
37 Noid, D. W., Sumpter, B. G., Varma-Nair, M. and Wunderlich, B. *Makromol. Chem., Rapid Commun.* 1989, **10**, 377
38 Noid, D. W., Sumpter, B. G. and Wunderlich, B. *Macromolecules* 1990, **23**, 664
39 Sumpter, B. G., Noid, D. W. and Wunderlich, B. *J. Chem. Phys.* 1990, **93**, 6875
40 Noid, D. W., Sumpter, B. G., Wunderlich, B. and Pfeffer, G. A. *J. Comp. Chem.* 1990, **11**, 236
41 Noid, D. W., Sumpter, B. G. and Cox, R. L. *J. Com. Polym. Sci.* 1991, **1**, 161
42 Zerbi, G., Magni, R., Gussoni, M., Moritz, K. H. and Sirlikov, S. *J. Chem. Phys.* 1981, **75**, 3175
43 Snyder, R. G., Maroncell, M., Strauss, H. L., Elliger, C. A., Cameron, D. C., Casal, H. L. and Mantsch, H. H. *J. Am. Chem. Soc.* 1983, **105**, 133
44 Snyder, R. G. *J. Chem. Phys.* 1967, **47**, 1316
45 Pan, R., Varma-Vair, M. and Wunderlich, B. *J. Therm. Anal.* 1989, **35**, 955